

Research Articles | Systems/Circuits

Cardiac-sympathetic contractility and neural alpha-band power: cross-modal collaboration during approach-avoidance conflict

<https://doi.org/10.1523/JNEUROSCI.2008-23.2024>

Received: 24 October 2023

Revised: 9 August 2024

Accepted: 26 August 2024

Copyright © 2024 the authors

This Early Release article has been peer reviewed and accepted, but has not been through the composition and copyediting processes. The final version may differ slightly in style or formatting and will contain links to any extended data.

Alerts: Sign up at www.jneurosci.org/alerts to receive customized email alerts when the fully formatted version of this article is published.

1 **Cardiac-sympathetic contractility and neural alpha-band power: cross-modal**
2 **collaboration during approach-avoidance conflict**

3
4 Abbreviated title: Contractility-alpha interactions in approach-avoidance

5
6 Neil M. Dundon^{*,1,2}, Alexander Stuber^{1,5}, Tom Bullock^{1,5}, Javier O. Garcia³, Viktoriya
7 Babenko^{1,5,7}, Elizabeth Rizer^{1,5,6}, Dengxian Yang^{4,5}, Barry Giesbrecht^{1,5,6}, Scott T. Grafton¹

8
9 ¹Department of Psychological & Brain Sciences, University of California, Santa Barbara, CA
10 93106, U.S.A.

11 ²Department of Child and Adolescent Psychiatry, Psychotherapy and Psychosomatics,
12 University of Freiburg, 79104 Freiburg, Germany

13 ³ Humans in Complex Systems Division, US DEVCOM Army Research Laboratory, Aberdeen
14 Proving Ground, MD 21005, U.S.A.

15 ⁴Department of Computer Science, University of California, Santa Barbara, CA 93106, U.S.A.

16 ⁵Institute for Collaborative Biotechnologies, University of California, Santa Barbara, CA 93106,
17 U.S.A.

18 ⁶Interdepartmental Graduate Program in Dynamical Neuroscience, University of California,
19 Santa Barbara, CA 93106, U.S.A.

20 ⁷BIOPAC Systems Inc., Goleta, CA 93117, U.S.A.

22 Correspondence: neil.dundon@psych.ucsb.edu

23 The authors declare no financial interests nor conflicts of interest.

24 **Abstract**

25

26 As evidence mounts that the cardiac-sympathetic nervous system reacts to challenging cognitive
27 settings, we ask if these responses are epiphenomenal companions or if there is evidence
28 suggesting a more intertwined role of this system with cognitive function. Healthy male and female
29 human participants performed an approach-avoidance paradigm, trading off monetary reward for
30 painful electric shock, while we recorded simultaneous electroencephalographic (EEG) and
31 cardiac-sympathetic signals. Participants were reward sensitive, but also experienced approach-
32 avoidance "conflict" when the subjective appeal of the reward was near equivalent to the revulsion
33 of the cost. Drift-diffusion model parameters suggested that participants managed conflict in part
34 by integrating larger volumes of evidence into choices (wider decision boundaries). Late alpha-
35 band (neural) dynamics were consistent with widening decision boundaries serving to combat
36 reward-sensitivity and spread attention more fairly to all dimensions of available information.
37 Independently, wider boundaries were also associated with cardiac "contractility" (an index of
38 sympathetically mediated positive inotropy). We also saw evidence of conflict-specific
39 "collaboration" between the neural and cardiac-sympathetic signals. In states of high conflict, the
40 alignment (i.e., product) of alpha dynamics and contractility were associated with a further
41 widening of the boundary, independent of either signal's singular association. Cross-trial
42 coherence analyses provided additional evidence that the autonomic systems controlling cardiac-
43 sympathetics might influence the assessment of information streams during conflict by disrupting
44 or overriding reward processing. We conclude that cardiac-sympathetic control might play a

45 critical role, in collaboration with cognitive processes, during the approach-avoidance conflict in
46 humans.

47

48 **Significance statement**

49 Complex behavior likely involves coordination across multiple branches of the human nervous
50 system. We know much of how cortical systems of the brain adapt to cognitive challenges. In
51 parallel, we are beginning to understand that autonomic mediated responses in peripheral
52 organ (cardiac-sympathetic) systems might also play an adaptive role in cognition, particularly
53 complex decisions. We probed if such signals have separate or collaborative associations with
54 behavior, using computational models of decision behavior, brain (electroencephalography) and
55 cardiac-sympathetic (contractility) data. Our evidence suggests that these systems might work
56 together, as humans attend to all available information when resolving particularly conflicting
57 decisions. The cardiac-sympathetic system may be part of a coordinated response that helps
58 balance the human tendency to overly focus on rewards.

59

60

61

62

63

64

65

66

67

68

69

70 **Introduction**

71

72 Our nervous system and coupled body evolved together to be flexibly responsive, allowing rapid
73 and often anticipatory changes to meet a broad array of cognitive and physical challenges
74 presented in dynamic environments. Decades of research in cognitive neuroscience have
75 characterized flexible cognitive mechanisms and underlying cortical systems for preserving goal-
76 directed function when external circumstances change. Meanwhile, autonomic reactivity in
77 peripheral organ systems, such as the cardiac-sympathetic branch, is well documented in tasks
78 requiring momentary goal-directed changes in mental and physical exertion, showing appropriate
79 reactivity (just enough, just in time) to tasks at hand (Richter et al., 2008; Richter et al., 2016;
80 Stump et al., 2023). More recent evidence extends cardiac-sympathetic reactivity to complex
81 cognitive

82 challenges such as value-based decision making (Dundon et al., 2020, 2021). However, it
83 remains unclear whether these peripheral responses are independent of cortically mediated
84 cognition or if the regulatory systems controlling these responses are more integrally involved in
85 cognitive processes. A crucial next step is to therefore pinpoint the specific cognitive mechanisms
86 that the cardiac-sympathetic system aligns with.

87

88 Emerging event-related evidence suggests cardiac-sympathetic reactivity might be particularly
89 relevant in value-based situations that involve some manner of "conflict" and where decisions

90 must incorporate negative information or costs (Ogden et al., 2019; Dundon et al., 2020; Dundon
91 et al., 2021). While such a reactivity profile could be epiphenomenal, it is also consistent with a
92 broader literature showing sympathetic involvement when humans face increasing uncertainty
93 (Palacios-Filardo and Mellor, 2019) and difficulty (Richter et al., 2008), or a requirement to explore
94 alternative goal-relevant stimuli (Aston-Jones and Cohen, 2005) with a specific emphasis on
95 incorporating negative information (Garrett et al., 2018). Together, these findings suggest cardiac-
96 sympathetic reactivity reflects a process that may be centrally generated and part of a coordinated
97 response that helps balance the human tendency to overly focus on rewards (Garrett et al., 2014;
98 Sharot and Garrett, 2016; Pedersen et al., 2021). However, to date, no study has tracked the
99 computational-behavioral and neural processes relevant for value-based conflict and reward
100 sensitivity, and thereafter probed whether reactivity in cardiac-sympathetics is independently or
101 collaboratively associated with behavior or cortical activity.

102
103 In the present work we therefore use a modified version of the approach-avoidance paradigm
104 (Champion, 1961; Elliot and Thrash, 2002). This paradigm creates states of high "conflict" when
105 the appeal of a reward is near equivalent to the revulsion of a cost (Figures 1A–B). It can also
106 identify sensitivity toward a particular value dimension, such as reward sensitivity (Volz et al.,
107 2017; Shapiro and Grafton, 2020; Pedersen et al., 2021; Figure 1C). We configured the paradigm
108 to additionally record how neural perceptual signals measured by electroencephalography (EEG)
109 track reward and cost information, specifically sensory gain (steady-state visually evoked
110 potentials; SS; Pfurtscheller and Aranibar, 1977; Galloway, 1990; Müller et al., 1998; Müller et al.,
111 2006; Gulbinaite et al., 2019) and goal-directed attention (spatially responsive dynamics in the
112 alpha band; Foxe and Snyder, 2011; Klimesch, 2012; Wang et al., 2016). We simultaneously
113 recorded beat-by-beat estimates of contractility (inotropy), which is primarily mediated by
114 noradrenergic sympathetic drive (after adjusting for heart and respiratory rate) and associated

115 with cardiac reactivity to challenge (Lewis et al., 1974; Light, 1985; Linden, 1985; Newlin and
116 Levenson, 1979; Sherwood et al., 1986, 1990; Callister et al., 1992). To further decompose
117 behavior, and extract fine-grained assays of behavior to correlate with physiology signals, we
118 fitted the drift-diffusion model (DDM) to choice and response time (RT) data (Figure 1D). Initially
119 considered in perceptual contexts (Usher and McClelland, 2001; Ratcliff and McKoon, 2008;
120 Forstmann et al., 2016), parameters from the DDM are an increasingly useful tool for
121 disambiguating the underlying reasons for lengthier RT in more complex value-based contexts
122 (Peters and D'Esposito, 2020; Shahar et al., 2019; Ballard and McClure, 2019; Colas, 2017;
123 Fontanesi et al., 2019; Dundon et al., 2023; Figure 1D).

124
125 [Figure 1 here]
126

127 Our primary aim was to establish how human participants respond to conflict at the computational-
128 behavioral level. We thereafter tested if cardiac-sympathetics are associated with relevant DDM
129 parameters in a manner that suggests redundancy (i.e., epiphenomenal), independent function
130 or collaboration (i.e., interaction) with perceptual neural signals. In particular, we examined if
131 cardiac-sympathetics aligned with neural processes associated with reward sensitivity, i.e.,
132 increased gain of or attention toward either cost information or more symmetric processing of
133 reward and cost.

134 135 136 **Materials and Methods**

137

138 We recorded continuous multi-channel electroencephalography and cardiac-sympathetic
139 physiology (combined electrocardiography and impedance cardiography) while human
140 participants made approach-avoidance choices regarding offers that varied trial-by-trial in reward
141 and in cost. Each "take-it-or-leave-it" trial offer gradually presented a monetary reward ranging in
142 value from \$0.01 to \$1.50 and a shock cost ranging in value from minimal to near maximum
143 bearable pain (see trial schematic in Figure 2A). We configured the paradigm to additionally
144 record how EEG signals track reward and cost information, both in terms of sensory gain (steady-
145 state visually evoked potentials; Figure 3A) and goal-directed attention (spatially responsive
146 dynamics in the alpha band; Figure 3B). We additionally divided neural assays into early and late
147 time windows, to capture the dynamics of conflict as decisions unfold, given recent evidence that
148 they might be time-sensitive Shapiro and Grafton (2020).

149

150 *Participants*

151 We recruited an initial sample of 33 human participants, via both word-of-mouth and an online
152 participant recruitment portal operated by the University of California, Santa Barbara (UCSB). We
153 removed six participants from all analyses: One subject accepted more than 90% of offers, two
154 participants' EEG data had an artefact in more than 50% of epochs, and one further subject
155 satisfied both screening criteria. In addition, we removed two participants due to excessive noise
156 in their impedance cardiography data. We accordingly report findings from a final sample of 27
157 participants. This group had a mean (standard deviation) age of 21.4 (3.3), and 17 were female.
158 All participants were right-handed and attested to no history of cardiovascular or related diseases.
159 Subject remuneration was \$20 per hour base rate, with a bonus payment determined by their
160 approach-avoidance behavior, which approximately corresponded to an additional \$13.50 per
161 subject. All testing took place during a single session in a quiet, dimly lit experimental suite and

162 all procedures received approval from the Institutional Review Board at UCSB. Participants
163 provided informed written consent, prior to participating.

164

165 *Approach-avoidance paradigm*

166 *Overview.* We used a modified version of the approach-avoidance task previously employed in
167 nonhuman primate (Amemori and Graybiel, 2012, 2015) and human (Volz et al., 2017; Shapiro
168 and Grafton, 2020; Dundon et al., 2021) experiments. The main modification was the
169 incorporation of reward and cost stimuli with different frequency flicker rates and spatial
170 positioning to facilitate identification of specific cortical activity. Stimuli also appeared gradually
171 on each trial, to facilitate identification of early and late responses. (O'Connell et al., 2012). Similar
172 to prior studies, participants approached or avoided varying levels of monetary reward paired with
173 varying levels of painful electric shock, in trial-by-trial "take-both-or-leave-both" offers. Participants
174 made a total of 352 approach-avoidance choices (split into eight blocks of 44). Their head position
175 was fixed by an adjustable chin and forehead rest, to maintain a viewing distance of 57 cm from
176 the stimulus presentation screen: an ASUS VS278 monitor, viewing area 60 cm width by 33.5 cm
177 height, refresh rate of 240 Hz (inter-frame interval=.004 s). We advised participants to move their
178 bodies as little as possible, to prevent motion-related confounds entering the physiology
179 recordings.

180

181 *Trial structure.* Each approach-avoidance trial gradually presented an offer to participants, in
182 which two bars communicating the level of reward and cost slowly appeared. Responses were
183 recorded with button press. The trial schematic is depicted in Figure 2A. During each trial,
184 participants fixated their eyes on a central point ($RGB_{[\min=0, \max=1]}=[.750 \ .750 \ .750]$;
185 diameter=0.221°). The background color remained black ($RGB_{[\min=0, \max=1]}=[0 \ 0 \ 0]$) at all times,

186 except for payout trials (see below). Offers comprised four sequential events: (i) baseline, (ii) offer
187 onset, (iii) offer offset and (iv) feedback. (i) Each offer initiated with a baseline period with a
188 duration between 420 and 540 frames (inclusive) drawn with discrete uniform probability on each
189 trial (approx. 1.75 s to 2.25 s). Baseline onset was signified by the immediate appearance of two
190 vertically oriented rectangular dot arrays, each spanning 7.30° width by 27.8° height, comprised
191 of 79 columns and 322 rows of dots (dot diameter=.056°), with centroids positioned at a horizontal
192 eccentricity +/- 3.75° from the central fixation point. (ii) Following baseline, during offer onset, the
193 offer bars gradually communicated the magnitude of the offer's value dimensions, with one bar
194 communicating the level of offered reward and the other bar communicating the level of incurred
195 shock. We drew a different offer on each trial from a two-dimensional decision (reward-by-shock)
196 space with uniform probability, and communicated the magnitude of each dimension by gradually
197 filling in an area of both bars with a relevant offer color (khaki or blue; one color per offer bar).
198 Specifically, contiguous rows of dots, equally portioned above and below the centroid of each
199 offer bar, gradually changed into one of two offer colors. The number of rows changing into an
200 offer color indicated the magnitude offered in that dimension, i.e., the offered reward (no rows:
201 \$0.01, to all rows: \$1.50) and the offered shock (no rows: minimum pain, to all rows: maximum
202 bearable pain—see "costs" section below). Counterbalanced across participants, reward and
203 shock mapped onto one color for the entire experiment, while color laterality was determined with
204 0.50 uniform probability before each trial. Offer onset duration was four seconds, with color
205 change controlled by reward and shock gradients that respectively changed dot colors from
206 baseline grey ($RGB_{[\min=0, \max=1]} = [.375 \ .375 \ .375]$) to peak offer color (khaki, $RGB_{[\min=0, \max=1]} = [.632$
207 $.586 \ .351]$; blue, $RGB_{[\min=0, \max=1]} = [.328 \ .616 \ .375]$) at even step sizes in RGB space over the offer
208 onset frames ($n=960$). (iii) Following peak onset, during offer offset, offer colors gradually returned
209 to baseline grey over a two-second period. We instructed participants to respond as soon as they
210 decided whether to approach or avoid an offer, with a time limit of the end of offer offset.

211 Participants registered their responses by pressing z with the index finger of their left hand, or m
212 with the index finger of their right hand. The mapping of z and m onto approach and avoidance
213 responses was fixed for each block of 44 trials, determined prior to the block with 0.50 uniform
214 probability. (iv) Following offer offset, participants observed a feedback screen for one second
215 (nine seconds for payout trials, see below). As depicted in the lower portion of Figure 2A, a
216 "successful" response, i.e., a single response executed during offer onset or offset, led to a
217 confirmation feedback screen containing a snapshot image of the offer (at peak offer colors),
218 accompanied by a written confirmation of their choice. If participants responded more than once,
219 responded during the baseline (pre-onset), or failed to execute any response before the final
220 frame of offer offset, a warning appeared on the screen indicating the relevant error, along with
221 the lateralized response prompts (lower portion of Figure 2A). We stored all error trials and
222 reissued them to participants after the eighth block, to ensure that errors could not be a strategy
223 to circumvent specific offers. All feedback screens (successful, error or payout (below)) also
224 included prompts to remind participants which colors mapped onto the different reward
225 dimensions (indicated with a lightning bolt (shock) or dollar symbol (reward) overlaying the
226 relevant bar), and which button response mapped onto which choice for the given block. This
227 screen was also displayed prior to each block. Finally, offer bars flickered throughout each trial,
228 either left: 12 Hz, right: 13.33 Hz or vice versa, determined with 0.50 uniform probability. We
229 presented all stimuli with customized scripts in MATLAB (Version 2018a, The Mathworks Inc.,
230 Natick, MA, USA, <https://www.mathworks.com/products/matlab.html>) using functions from
231 PsychToolbox-3 (Brainard, 1997; Pelli, 1997; Kleiner et al., 2007). Successfully registered choices
232 were coded either 1 (approach) or 0 (avoid), and response time (RT) was the time (in seconds)
233 between offer onset and choice execution.

234

235 *Costs:* Shocks offered to each participant were calibrated a priori in order to range in pain from
236 an individualized subjective minimum to near-maximum level. We administered the costs with
237 cutaneous electrical stimulation (1 s duration; $f=100$ Hz; $\lambda=2$ ms), via two electrodes on the back
238 of the hand. We used a constant current stimulator and train generator (respectively, models
239 DS7A and DG2A, Digitimer, Great Britain), and modulated pain via voltage. We used an identical
240 calibration procedure to previous studies (Shapiro and Grafton, 2020; Dundon et al., 2021). That
241 is, we started 1 mV and gradually increased voltage until participants reported (1) a perception of
242 the shock, then (2) when the voltage began to cause discomfort, and then finally (3) when the
243 voltage caused unbearable pain. Once a level of unbearable pain was reported, we asked them
244 to confirm that this was the maximum pain they could tolerate. This prompt usually spurred
245 participants to accept a further increase in voltage. Once they confirmed reaching an unbearable
246 level of pain, we administered 14 sample shocks, ranging in voltage between (2) and (3) above,
247 and participants reported the level of pain on a scale of 0 to 10. We repeated this entire procedure
248 twice to account for habituation. Shocks offered to each participant then ranged from a lower
249 bound of (2) above to an upper bound of the second estimate of (3) above. We also fitted a
250 sigmoid function to the second set of pain ratings, to first estimate shocks of 0.05, 0.25, 0.50,
251 0.75, and 0.95 intensity (as per their individualized scales) to provide as sample shocks. We also
252 estimated where their 0.80 level of pain was and excluded trials offering pain equal or greater to
253 this level from payout trials (see below).

254

255 *Payout trials.* For safety reasons, we did not administer any electric shocks during the testing
256 session while participants wore physiology electrodes. We instead postponed payout on an
257 infrequent subset of trials, in line with previous work recording physiology signals during similar
258 approach-avoidance paradigms (Shapiro and Grafton, 2020; Dundon et al., 2021). Prior to testing,
259 we selected eighteen "payout trials" (5.11%) with uniform probability across the entire set of offers,

260 provided the offered shock was below 80% of a subject's maximum pain level. The baseline,
261 onset and offset sequence of payout trials were identical to non-payout trials. However, during
262 the feedback section of payout trials (extended from one to nine seconds), the screen changed
263 from black to red ($RGB_{[\min=0, \max=1]}=[1\ 0\ 0]$; left lower portion of Figure 1C) and participants learned
264 that the monetary reward and shock from that offer would be administered following the testing
265 session (were that offer approached) or that the values would have been administered (were that
266 offer avoided). If participants made a response error during a payout trial, they instead saw the
267 error feedback screen, and the payout trial was added to the list of trials to be reissued. We
268 instructed participants that payout trials could not be predicted before registering a response and
269 to treat each offer as a potential payout trial. Previous work reports that payout trials do not affect
270 behavior on subsequent choices (Shapiro and Grafton, 2020; Dundon et al., 2021).

271
272 *Paradigm configuration for perceptual signals.* We configured the paradigm to record how neural
273 perceptual signals measured by EEG track reward and cost information, both in terms of sensory
274 gain (steady-state visually evoked potentials; Figure 3A) and goal-directed attention (spatially
275 responsive dynamics in the alpha band; Figure 3B). The former was achieved by flickering the
276 offer bars throughout each trial, one at 12 Hz, the other at 13.33 Hz. This meant that each trial
277 had a unique frequency "tag" associated with reward and cost. For the latter, we lateralized the
278 reward and cost stimuli to exploit spatially responsive alpha dynamics. For the specific filtering
279 procedure in each case, see the *Neural recordings* section below.

280
281 *Behavioral analyses*

282 *Overview.* We performed initial behavioral analyses to evaluate whether participants were reward
283 sensitive in addition to whether they confronted approach-avoidance "conflict" in established

284 regions of decision space when performing our task. To conform with previous studies, we used
285 a logistic framework employing maximum-likelihood methods to compute subjective value and all
286 related measurements. All other modeling and statistical tests were performed using hierarchical
287 Bayesian models, in which posteriors were sampled and model fits computed using a combination
288 of HDDM (Wiecki et al., 2013) and pymc3 functions (Salvatier et al., 2016) in Python.

289

290 *Logistic choice models.* We used a logistic framework previously reported (Shapiro and Grafton,
291 2020; Dundon et al., 2021). This framework fits two-dimensional logistic models separately to
292 each individual subject's set of choices (Y), modeling p(approach) as a function of the
293 corresponding set of rewards (X1) and shock costs (X2) offered, with a standard logit function,
294 i.e.:

295

296

$$Y = \text{logit}^{-1}(b_0 + b_1 * X1 + b_2 * X2).$$

297

[Eq. 1]

298

299 We estimated the maximum likelihood parameters of each participant's model using the `mnrfit`
300 function in MATLAB after first normalizing X1 and X2 to z-score ranges within participants.

301

302 *Reward sensitivity* in approach-avoidance contexts is demonstrated by choices that overweight
303 the reward relative to the offered costs (Figure 1C). In our paradigm we uniformly sampled the
304 reward and cost dimensions, the latter of which was calibrated to span an individualized minimum
305 to maximum (see above section on "Costs" in the section describing the paradigm). We
306 accordingly deduce that participants were reward sensitive within this task context if their logistic

307 choice coefficients (from Eq. 1) showed a bias toward approach ($b_0 > 0$) or an overweighting of the
308 reward coefficient ($|b_1| > |b_2|$).

309

310 *Approach-avoidance conflict* is highest near the region of decision space where participants are
311 as likely to approach as they are to avoid (Figure 1A). We assessed the level of conflict presented
312 by each trial, accounting for individual differences in subjective valuations, using a previously
313 employed procedure (Shapiro and Grafton, 2020; Dundon et al., 2021). The method uses discrete
314 classification, categorizing trials as either high or low in conflict. For this, from the coefficients of
315 each participant's logistic choice model (from Eq. 1), we first computed the subjective value (the
316 log odds of approach) of each trial as $SV_k = b_0 + b_1 * x_{1k} + b_2 * x_{2k}$, where x_{1k} and x_{2k} are respectively
317 the reward and cost offered on trial (k), normalized to z-score ranges within participants. In this
318 way $SV > 0$ reflects $p(\text{approach}) > 0.50$ and vice-versa. We then classified a trial as high conflict if
319 it was either (a) approached, but where its SV_k was below the median SV of all approached trials,
320 or (b) avoided, but where its SV_k was above the median SV of all avoided trials. These trials are
321 depicted schematically by the fuchsia regions in Figure 1. All remaining trials were classified as
322 low conflict, depicted by the aqua regions in Figure 1. For each trial, its SV and its binary degree
323 of conflict (high vs low) were estimated prior to any screening due to EEG or sympathetic artefact,
324 described in the section below.

325

326 We performed additional tests to support that the logistic framework had identified states of high
327 and low conflict. One indication of high conflict is a reduction in choice "consistency". For this, we
328 used a nonparametric assessment of the deviation in choices appearing in bins of the decision
329 space. We divided each participant's decision space into a ten-by-ten grid of equal bins. We
330 enumerated choice consistency for a given bin as the variance in choices across all offers

331 appearing in it. Choices were numerically assigned $x=0$ for avoid and $x=1$ for approach, and
332 variance (V) computed across n trials in each bin as $V_{\text{bin}} = \frac{1}{n} \sum_{k=1}^n (x_k - \bar{x})^2$. Positive variance values
333 reflect lower consistency (i.e., different choices registered at different times for similar offers). We
334 compared (between participants) regions identified as high and low conflict (see above) using
335 each participant's average consistency score across all bins in a region. An additional indication
336 of high conflict is lengthier RT which we defined as the time between the onset of the offer and
337 the registration of a response. We accordingly compared (between participants) trials identified
338 as high and low conflict, comparing participants' region specific median RT.

339

340 *Computational modeling framework*

341 *Overview.* Our computational modeling aimed to assess whether states of high conflict shaped
342 parameters associated with choice behavior, and whether key parameters were additionally
343 associated with trial-by-trial fluctuations in neural signals, a cardiac-sympathetic signal or the
344 alignment (interaction) of neural and cardiac signals.

345

346 *HDDM.* We decomposed behavior using a Hierarchical-Bayesian extension of the drift-diffusion
347 model (DDM; Figure 1D). The DDM classically proposes that choice and RT data are underscored
348 by a noisy evidence accumulation process that terminates at a decision criterion (boundary).
349 Following an initial nondecision time (t), the decision process begins at starting point (z) and
350 accumulates evidence at rate (v) toward one of two boundaries that determines the choice (in our
351 case, approach (+) or avoid (-)); boundaries are separated by distance (a). These parameters
352 provide a fine-grained assay of behavior, such as likely bias toward one choice (z), how rapidly
353 evidence is integrated during decision formation (v) or the amount of evidence required before a
354 choice is executed (a wider boundary denoting a more conservative criterion). With the

355 Hierarchical-Bayesian extension (HDDM; Wiecki et al., 2013), the choice and RT data of each
356 trial (y_t) form a distribution described by a Wiener diffusion likelihood function (Navarro and Fuss,
357 2009), parameterized by $\{a,v,t,z\}$. These parameter posteriors can be sampled in a static fashion
358 using Bayes Monte Carlo, i.e.:

359

360

$$y_k \sim \text{Wiener}(a,v,t,z)$$

361

[Eq. 2]

362

363 A wealth of existing literature has tested hypotheses by additionally fitting the DDM parameters
364 separately for different task conditions (e.g. Ratcliff and Frank, 2012; Wiecki et al., 2013;
365 Bottemanne and Dreher, 2019; reviews in O'Connell et al., 2018; Gupta et al., 2022). Under the
366 above probabilistic framework, parameters $\{a,v,t,z\}$ can be fitted as a mixture model, to account
367 for different states (s). In such a case, the model assigns y_k to one of two Wiener distributions,
368 depending on trial k 's state of conflict (s), i.e.:

369

370

$$y_k | (s_k=s) \sim \text{Wiener}(a_s, v_s, t_s, z_s)$$

371

[Eq. 3]

372

373 where $s \in \{0,1\}$, i.e., low or high conflict. Evaluating this mixture extension allows probabilistic
374 inference that DDM parameters are credibly different depending on the state of conflict. This can
375 be evaluated using model fits and/or by testing whether the highest density interval (HDI) of the

376 group-level posterior for a parameter in low conflict ($s=0$) minus the posterior for that parameter
377 in high conflict ($s=1$) does not subtend 0, i.e., $0 \notin \text{HDI}([p(P_0|y_0)] - [p(P_1|y_1)])$, where $P \in \{a, v, z, t\}$.

378

379 Under the probabilistic framework, parameters $\{a, v, t, z\}$ can additionally be modeled as a linear
380 combination of continuous predictors, such as trial-by-trial estimates of a neural (e.g., Frank et
381 al., 2015) or cardiac-sympathetic signal, i.e.:

382

383 $y_k \sim \text{Wiener}(a, v, t, z)$, where:

384
$$a = b_{0,a} + b_{1,a} * X_1, \dots, b_{n,a} * X_n$$

385
$$v = b_{0,v} + b_{1,v} * X_1, \dots, b_{n,v} * X_n$$

386
$$t = b_{0,t} + b_{1,t} * X_1, \dots, b_{n,t} * X_n$$

387
$$z = b_{0,z} + b_{1,z} * X_1, \dots, b_{n,z} * X_n$$

388 [Eq. 4]

389

390 Here, X_1, \dots, X_n are vectors of trial-by-trial physiology signals and $b_{1,P}, \dots, b_{n,P}$ are their coefficients
391 (for each $P \in \{a, v, t, z\}$). Evaluating this regression extension (either using model fits or by testing if
392 the HDI of group-level posteriors $b_{1,P}, \dots, b_{n,P}$ do not contain 0) allows probabilistic inference that
393 DDM parameters are associated with moment-to-moment physiological fluctuations.

394

395 Finally, the models described in Eqs. 3 and 4 can be merged into a mixed-regression model, to
396 allow inference about both state-specific parameter estimates and state-specific associations
397 between moment-to-moment physiology and parameters, i.e.:

398

399

$y_k|(s_k=s) \sim \text{Wiener}(a_s, v_s, t_s, z_s)$, where:

400

$$a_s = b_{0,a,s} + b_{1,a,s} * X_{1,s}, \dots, b_{n,a,s} * X_{n,s}$$

401

$$v_s = b_{0,v,s} + b_{1,v,s} * X_{1,s}, \dots, b_{n,v,s} * X_{n,s}$$

402

$$t_s = b_{0,t,s} + b_{1,t,s} * X_{1,s}, \dots, b_{n,t,s} * X_{n,s}$$

403

$$z_s = b_{0,z,s} + b_{1,z,s} * X_{1,s}, \dots, b_{n,z,s} * X_{n,s}$$

404

[Eq. 5]

405

406 Here $X_{1,s}, \dots, X_{n,s}$ are vectors of trial-by-trial physiology signals in state s . Evaluating this mixture-
407 regression extension allows the inferences of Eqs. 3 and 4. In addition, this model allows
408 probabilistic inference about whether the association between DDM parameters and physiological
409 fluctuations depends on the state of conflict.

410

411 In our analyses, we used an iterative approach to narrow down the best combination of physiology
412 variables associated with state-specific parameters of the DDM. We first fitted a "baseline" model.
413 This was the mixture model described in Eq. 3 and it both served as a baseline comparison for
414 later physiology models and probed the static parametric differences between high and low
415 conflict (Figure 2D). We then fitted a series of mixture-regression models using the formula in Eq.
416 5. These models tested if additionally modeling the state-specific parameters as a linear

417 combination of a state-specific physiology signal would provide a better-fitting model than the
418 baseline. These "singular" models (Figure 3D) contained a single regressor, i.e.:

419

420

$$P_s = b_{0,P,s} + b_{1,P,s} * X_{1,s} \text{ for each } P \in \{a, v, z, t\}$$

421

[Eq. 6]

422

423 where $s \in \{0, 1\}$, i.e., low or high conflict, and the single regressor ($X_{1,s}$) was one of the neural
424 variables, or the cardiac-sympathetic variable, described below. We used model fits (Deviance
425 Inference Criterion (DIC); Wiecki et al., 2013) to determine if these singular models were a better
426 fit to the data than the baseline model.

427

428 We pre-empt some results here to aid describing the next stage of modeling, i.e., that a number
429 of singular models were superior fits to baseline, including the singular model containing the
430 cardiac-sympathetic assay. We next fitted a series of "cross-modal" mixture-regression models
431 (Figure 3E). These models tested whether the best singular model fit could be improved by
432 extending it to two regressors. In each of these models, one regressor was the cardiac-
433 sympathetic assay and the other regressor was a neural variable (i.e., cross-modal). We restricted
434 the addition of neural variables to only those that had featured in singular models that were
435 superior fits to baseline. A two-regressor "additive" cross-modal model was therefore:

436

437

$$P_s = b_{0,P,s} + b_{1,P,s} * X_{1,s} + b_{2,P,s} * X_{2,s} \text{ for each } P \in \{a, v, z, t\}$$

438

[Eq. 7]

439

440 Here $s \in \{0, 1\}$, i.e., low or high conflict, the first regressor ($X_{1,s}$) was the cardiac-sympathetic assay
441 and the second regressor ($X_{2,s}$) was a neural variable from singular models outperforming
442 baseline. An additional three-regressor "interactive" cross-modal model was:

443

444

$$P_s = b_{0,P,s} + b_{1,P,s} * X_{1,s} + b_{2,P,s} * X_{2,s} + b_{3,P,s} * X_{3,s} \text{ for each } P \in \{a, v, z, t\}$$

445

[Eq. 8]

446

447 Here all parameters were the same as in Eq. 7, except now a third regressor ($X_{3,s}$) contained the
448 z-score-normalized dot product of $X_{1,s}$ and $X_{2,s}$, i.e., capturing the correlation over trials between
449 the neural and cardiac variable. In other words, the interactive model additionally allowed
450 inference about the alignment of neural and cardiac signals being associated with DDM
451 parameters. We used model fits DIC scores to determine if any additive (Eq. 7) or interactive (Eq.
452 8) models were a better fit to the data than the best-fitting singular model (Eq. 6).

453

454 We pre-empt some additional results here to aid describing the next stage of modeling, i.e., that
455 a number of cross-modal models were superior fits to the best-fitting singular model. We next
456 fitted a final series of mixture-regression models (Figure 3F). These "complement" models now
457 tested whether the best-fitting cross-modal model could be improved by extending it to incorporate
458 additional neural regressors and regressors of neural-cardiac alignment. The design matrix of
459 these models started with the regressors from the best-fitting cross-modal model, i.e., a neural
460 variable, the cardiac-sympathetic variable and, if applicable, the interaction term. We then tested
461 if the fit could be improved by also including complement (i.e., set difference) regressors from

462 other cross-modal models. In other words, we combined cross-modal design matrices, removing
463 redundant regressors. We tested complement models by merging the best-fitting cross-modal
464 model with the set difference of the cross-modal models involving all neural variables that passed
465 the singular model stage (i.e., early_attn_rew, late_the, early_SS_sym, late_alpha_sym,
466 late_alpha_rew), using their best-performing cross-modal forms (i.e., whether or not they included
467 interactions). Each "complement" model was therefore:

$$P_s = B * [X'_{P,s} | X''_{P,s} \setminus X'_{P,s}] \text{ for each } P \in \{a, v, z, t\}$$

[Eq. 9]

472 where $s \in \{0, 1\}$, i.e., low or high conflict, X' is the design matrix of the best-fitting cross-modal
473 model, X'' is the design matrix of an additional cross-modal model (provided it was a superior fit
474 to the best singular model) and $X'' \setminus X'$ describes the set-difference, i.e., removal of any common
475 columns between them. B is a coefficient vector of length corresponding to the resulting
476 concatenated design matrix. We used model fits DIC scores to determine if any complement
477 models (Eq. 9) were a better fit to the data than the best-fitting cross-modal models (Eqs. 7–8).

479 *Model to discretize neural-cardiac interactions.* We pre-empt some additional results here to aid
480 describing the next stage of modeling, i.e., that one complement model was a superior fit to the
481 best-fitting cross-modal model. This model featured an association between the decision
482 boundary and a dot-product regressor described in the "interactive" model in Eq. 8 (specifically
483 contractility · late α_{sym}). This association was additionally unique to states of high conflict. To
484 help clarify the underlying dynamics of this seeming three-way interaction, we fitted a model that

485 discretized these two continuous regressors (high and low contractility and high and low late
486 α_{sym}) within each participant, and fitted a decision boundary separately for the resulting
487 combination of physiological states, separately again for low and high conflict, creating eight
488 states in total. This model was the same as the baseline model in Eq. 3 but with a different
489 parameter mixture for the decision boundary, i.e.:

490

$$491 \quad y_k | (s_k=s, d_k=d) \sim \text{Wiener}(a_d, v_s, t_s, z_s)$$

492 [Eq. 10]

493

494 where $s \in \{0,1\}$, i.e., low or high conflict, and $d \in \{000,001,010,011,100,101,110,111\}$, where the
495 digits in each of the eight binary code sequences respectively describe the conflict (low (0) or high
496 (1)), late α_{sym} (low (0) or high (1)) and contractility (low (0) or high (1)) states of trial k . The
497 latter two levels were classified using median splits within participants. In this model, we report
498 parameter estimates a_d as a difference measure (Δ boundary) from when $d=000$.

499

500 *Control models for local and global brain activity.* To assess whether cardiac-sympathetics might
501 be a proxy for more general activity levels in the brain (for example, a global or frequency-specific
502 increase in gain), we performed two additional control models for our best-fitting complement
503 model. In each case, we substituted an alternative measure of brain activity for the contractility
504 regressor and the contractility component of any dot-product (interaction) regressors featuring
505 contractility. In the first, we substituted contractility with an estimate of global field power (GFP;
506 Skrandies, 1990), which we computed as the standard deviation across all electrodes in the
507 montage, with data bandpass-filtered from 1 Hz to 40 Hz. In the second, we substituted

508 contractility with a signal more local to the relevant frequency band in our findings (alpha). For
509 this, we used an estimate of the average alpha power across all electrodes in the montage, with
510 data preprocessed in the same way as our assays in this frequency band (see below). For a single
511 trial-by-trial estimate in each case, we averaged both the GFP measure (using the root-mean-
512 square average) and the global alpha power measure across timepoints in the time window [0 s
513 to 1 s] post offer onset.

514
515 In all HDDM models, we sampled both individual and group-level parameters in a hierarchical
516 fashion and report group-level findings. We sampled posteriors 5000 times with Markov-Chain
517 Monte Carlo, using the HDDMRegressor function from the HDDM toolbox (Wiecki et al., 2013)
518 version 0.6.0 in Python 2.7, using default settings for hyper-parameters. We discarded the first
519 500 samples of each posterior estimate as tuning steps. A single drift rate was fitted using a link
520 function that made it negative on avoid trials and positive on approach trials.

521
522 *Alternative model assessment.* For the baseline model, and for the best-fitting singular, cross-
523 modal, and complement models, we additionally report a proxy of RT variance explained by each
524 model using a bin-by-bin regression procedure. This procedure first simulated trial-by-trial RTs
525 using posterior medians of parameters of the models (linearly estimated where relevant using
526 model coefficients and trial-by-trial regressors) with a Wiener-like process. For approach trials,
527 the simulated decision process (x) initiated at time ($RT=0$) at a starting point in units of the
528 boundary, i.e., $x(RT=0)=z \cdot a$. As RT increased in units of 0.01, x increased with $x=x+0.01v$ until
529 the boundary was reached, i.e., $x>a$. For avoid trials, the process was the same except with v
530 inverted and the process continuing until $x<0$. Finally, nondcision time (t) was added to the
531 resulting RT to arrive at the final simulated value. We next binned observed RTs and correlated

532 bin-by-bin medians with medians derived from corresponding simulated RTs. We report variance
533 explained from Pearson correlations (R^2) for this procedure separately using 10, 15, 20, 25, 30,
534 35, and 40 bins of RT in the correlation.

535

536 *EEG neural recordings - Recording, preprocessing and assays*

537 *Recording.* Concurrent with the approach-avoidance paradigm, we recorded continuous
538 electroencephalogram (EEG) data from a montage of 63 scalp electrodes (channels) arranged
539 using the International 10-20 system. We sampled the EEG signal at 1000 Hz from each channel,
540 using a BrainAmp MR amplifier (Brain Products, Berlin, Germany). Channel FCz served as the
541 online reference while channel Cz served as the ground. Between blocks, experimenters paused
542 recordings to check electrode impedance ($<5\text{ k}\Omega$) and noisy channels.

543

544 *EEG preprocessing* used functions available in the EEGLAB toolbox (Delorme and Makeig, 2004).
545 First, each participant's EEG data were downsampled (250 Hz) and hi-pass filtered ($<1\text{ Hz}$)
546 separately for each block. Line noise was removed with an automated function (Mullen, 2012).
547 We merged resulting sets of blockwise data into a single set (one set per subject) and identified
548 noisy channels using an automated function that tested whether data in each channel correlated
549 with those in surrounding channels by a coefficient of at least 0.85 (Kothe and Makeig, 2013).
550 Identified channels were replaced using spherical interpolation. We then re-referenced datasets
551 to the montage average, created epochs spanning from -1 s to +6 s relative to offer onset, and
552 subtracted baseline means (taken from the window -.5 s to 0 s relative to offer onset). We then
553 performed ICA decomposition separately on each subject's resulting epochs, and stored the
554 resulting weights of components that were 95% likely to be ocular or cardiac activity, determined
555 by an automated classifier (Pion-Tonachini et al., 2019). We next imported, downsampled, hi-

556 pass-filtered and removed line noise from participants' separate blocks of raw data again, as
557 above. Separately for each block, we replaced noisy channels as above and removed ICA
558 components related to ocular and cardiac artefacts. We marked any data point where any channel
559 still exceeded 150 mV (for later rejection) and applied a spatial Laplacian filter across multichannel
560 data at each time point. We then reversed the laterality of electrodes on all trials where reward
561 appeared on the left of the screen, so that each trial "de facto" presented reward on the right and
562 cost on the left. We refer to data at this stage as "preprocessed" data.

563
564 *Assay of sensory gain.* To extract timeseries from preprocessed data for steady-state visually
565 evoked potentials relevant for reward (SS_{rew}) and cost (SS_{shk}) information (Figure 3A), we used
566 rectified and smoothed power timeseries that had been filtered to either 12 or 13.33 Hz, depending
567 on the flicker of reward or cost information for a given trial (note that no specific frequency mapped
568 onto either reward or cost; flickers varied trial-by-trial). We convolved each channel's fast-Fourier-
569 transformed data with trapezoid-shaped bandpass filters ("on" width = .5 Hz, transition bandwidth
570 = 0.25 Hz), centered on 12 Hz or 13.33 Hz before rectifying, smoothing (mean within sliding
571 windows spanning 66 ms) and downsampling inverse-Fourier timeseries to 125 Hz. We also
572 constructed a third dataset, using these exact procedures, but with filters centered on 12.66 Hz
573 (midway between 12 and 13.33 Hz), and subtracted it from SS_{rew} and cost SS_{shk} timeseries to
574 mitigate SS influence from underlying activity in the alpha band. We created epochs spanning
575 from -1 s to +6 s relative to offer onset for the 12 and 13.33 Hz datasets, removing the baseline
576 average value in the 500 ms window prior to offer onset. For trial-by-trial measures, we computed
577 the average power in early ([0 s to 1 s] post offer onset) and late ([1 s to 2 s]) time windows (Figure
578 3A). Amplitudes were averaged at electrode sites contralateral to the relevant information, i.e.,
579 O1 and PO1, or at electrodes O2 and PO2, depending on reward and cost laterality on a given
580 trial (Figure 3A).

581

582 *Assay of goal-directed attention.* We also extracted timeseries from preprocessed data of spatially
583 sensitive alpha power, i.e., relevant for reward (α_{rew}) and cost (α_{shk}) information (Figure
584 3B). We first applied notch filters to remove power in SS frequencies (inverse of bandpass filters
585 above), and then convolved each channel's fast-Fourier-transformed data with a trapezoid-
586 shaped bandpass filter ("on" segment spanning 7 Hz to 14 Hz, transition bandwidth = 0.5 Hz).
587 Resulting inverse-Fourier timeseries were rectified, smoothed (mean within sliding windows
588 spanning 66 ms) and we downsampled channels to 125 Hz. We created epochs spanning from -
589 1 s to +6 s relative to offer onset, removing the baseline average value in the 500 ms window prior
590 to offer onset. For trial-by-trial measures, we computed the average power in early ([0 s to 1 s]
591 post offer onset) and late ([1 s to 2 s]) time windows (Figure 3B). Amplitudes were averaged at
592 electrode sites contralateral to the relevant information, i.e., PO and PO7, or at electrodes PO2
593 and PO8, depending on reward and cost laterality on a given trial (Figure 3B).

594

595 *Symmetry timeseries.* In our approach-avoidance paradigm, conflict peaks when an offer's value
596 makes approaching it as appealing as avoiding it, measured as the absolute distance from a
597 decision boundary ($SV=0$ or $p(\text{approach})=0.50$; Figure 1). For both the SS and alpha timeseries
598 we also computed a neural proxy of conflict to include in our models, by way of a "symmetry"
599 timeseries, at each timepoint (t); i.e., $SS(t)_{sym}=-1*\log(|SS(t)_{rew}-SS(t)_{rew}|)$; $\alpha(t)_{sym}=-$
600 $1*\log|\alpha(t)_{rew}-\alpha(t)_{shk}|$. Given the inversion, higher values reflect higher symmetry, or in
601 other words, that more equal power was present in the traces relevant for reward and cost (Figure
602 3A–B). For trial-by-trial measures, we computed averages in the same manner (early and late
603 windows) as the single traces. To verify that these symmetry metrics tracked conflict, we
604 performed repeated-measures ANOVAs testing whether each participant's symmetry trace was

605 modulated by the state of conflict (low or high), the phase of trials (early vs late), or their
606 interaction.

607

608 *Assays of cognitive control and decision making.* The assays of neural activity described above
609 exploit the modifications (graded onset, frequency-tagged, spatially mapped stimuli) we made to
610 the approach-avoidance paradigm and allow comparison and contrast between early and late
611 perceptual processes during decision making. However, to perform a more complete analysis of
612 neural-cardiac-behavioral relationships, we additionally extracted neural signals traditionally
613 associated with other components that are likely relevant during the approach-avoidance conflict.
614 The first was delta power over posterior parietal sites (Figure 3C). Activity in this frequency range
615 has been linked with DDM-like mechanisms of decision making in perceptual contexts (O'Connell
616 et al., 2012; Harper et al., 2014). For trial-by-trial measures, we computed the average power
617 between (1 and 4 Hz) in early ([0 s to 1 s] post offer onset) and late ([1 s to 2 s]) time windows at
618 electrode sites (CPz and Cz). The other signal we extracted was frontal-midline theta (Figure 3C),
619 classically considered an assay of cognitive control and action regulation (Luu et al., 2004;
620 McLoughlin et al., 2014). For trial-by-trial measures, we computed the average power between (4
621 and 7 Hz) in early ([0 s to 1 s] post offer onset) and late ([1 s to 2 s]) time windows at electrode
622 sites (Fz, F1 and F2).

623

624 *Alpha-phase coherence.* In a final neural-cardiac analysis (as a follow-up on later-reported
625 results), we probed how the state of cardiac-sympathetics (specifically, whether contractility was
626 high or low) was related to the coherence of alpha power across trials, relevant to both the reward
627 and cost information. We re-processed the alpha-band activity contralateral to the reward and
628 cost information, extracting the phase angle of these waveforms over time, i.e., $\alpha_{\text{rew}\theta}$ and

629 $\alpha_{\text{shk}}\theta$. If specific events (such as the onset of an offer) evoked temporally consistent
630 fluctuations in alpha power, phase angles would summarize across trials to a coherent sinusoid-
631 like waveform oscillating in and around the alpha-band frequency (7–14 Hz). We averaged across
632 trials for each participant's $\alpha_{\text{rew}}\theta$ and $\alpha_{\text{shk}}\theta$ timeseries, separately for trials in states of high
633 and low conflict and separately again for trials in states of high and low contractility (determined
634 by a median split across all of a participant's trials). To compute a summary estimate of early and
635 late coherence across trials, we rectified the resulting participant-average phase waveforms $|\theta|$,
636 and computed the average values across datapoints in early ([0 s to 1 s] post offer onset) and
637 late ([1 s to 2 s]) time windows (Figure 5A).

638

639 *Cardiac-sympathetic recordings - Recording, preprocessing and contractility assay*

640 *Recording.* Concurrent with the approach-avoidance paradigm we also recorded data from
641 combined electrocardiogram (EKG) and impedance cardiogram (ICG) using a total of ten EL500
642 electrodes (BIOPAC, USA). Prior to recording, in a private room, a trained female researcher
643 disinfected the skin at the electrode sites. They gently exfoliated the skin with an abrasive pad
644 (ELPAD, BIOPAC, Inc.), applied NuPrep skin exfoliating gel (ELPREP, BIOPAC, Inc.) to each
645 electrode site (~1-by-1 inch area of skin) and fanned the sites dry. EKG was recorded from one
646 electrode beneath the right collarbone and one beneath the left rib cage. ICG was recorded from
647 eight electrodes: two on each side of the torso and two on each side of the neck. ICG electrodes
648 served as the ground for EKG. All electrodes had a small dab of electrode gel (GEL100, BIOPAC,
649 Inc.). The upper neck and lower torso (outside) electrodes injected a 4mA alternating current into
650 the thoracic cavity at 50 kHz, while the lower neck and upper torso (inner) electrodes were
651 voltage-sensing. We sampled both the EKG and ICG signals at 5000 Hz via carbon fiber leads
652 connected respectively to ECG100C and NICO100C amplifiers, integrated with an MP150 system

653 (BIOPAC, Inc.). Online, AcqKnowledge software version 4.3 differentiated the raw basal
654 transthoracic impedance (z) ICG data with respect to time (dz/dt) and removed respiratory artifact
655 from the ensuing dz/dt waveform with a high-pass filter (BIOPAC, Inc.). Once seated in the testing
656 suite, we instructed participants to minimize unnecessary movement and vocal sounds to limit
657 disruptions to the physiology signal. Participants completed a nonrecorded resting period to
658 acclimate to the study environment. Between blocks, experimenters paused recordings to check
659 for noise in the EKG and ICG data.

660
661 *EKG/ICG preprocessing and contractility assay.* We estimated contractility from the pre-ejection
662 period (PEP). We used a semi-automated software package (MEAP; Cieslak et al., 2018), which
663 uses moving ensemble averages (15-second windows) to help identify the R point of the EKG
664 QRS complex (early systole: initial left-ventricular depolarization) and the B point of the dz/dt
665 waveform from the ICG (mid systole: opening of the aortic valve), for each individual heartbeat
666 (Figure 3D); all heartbeats were manually checked for correct point classification. The time period
667 between these two cardiac events is the pre-ejection period (PEP). This electro-mechanical time
668 interval, covering systolic activity from the initial electrical depolarization of the left ventricle until
669 the opening of the aortic valve, is an index of beta-adrenergic contraction vigor, and is primarily
670 mediated by sympathetic activity (Lewis et al., 1974; Light, 1985; Linden, 1985; Newlin and
671 Levenson, 1979; Sherwood et al., 1986; 1990). Shorter intervals reflect increased contractility
672 (positive inotropy). For trial-by-trial measures, we computed the average PEP value across all
673 heartbeats occurring in the two-second window immediately following offer onset (Figure 3D).
674 These values were log-transformed and then reverse-scored, so that higher values reflect higher
675 contractility.

676

677

678 **Results**

679

680 We recorded continuous multi-channel electroencephalography and cardiac-sympathetic
681 physiology while 27 human participants performed an approach-avoidance task, trading off
682 monetary reward for electric shock cost (see trial schematic in Figure 2A). On average,
683 participants accepted 68% ($\sigma=12.6\%$) of offers, and responded with median RT of 1.73 seconds
684 ($\sigma=0.428$) relative to offer onset.

685

686 *Behavioral results*

687 *Logistic choice models.* From two-dimensional logistic models fitted separately to each individual
688 subject's set of choices, modeling $p(\text{approach})$ as a function of an intercept (b_0) and the magnitude
689 of monetary reward (b_1) and shock cost (b_2) offered on each trial, these two continuous value
690 dimensions respectively increased (group-mean $b_1=6.05$; $t(26)=9.55$; $p<0.001$, Figure 2B) and
691 decreased (group-mean $b_2=-4.76$; $t(26)=-7.65$; $p<0.001$, Figure 2B) the log odds of approach. In
692 other words, participants integrated both reward and a cost into their choices. However these
693 parameters also confirmed that participants were reward sensitive, characterized by a bias toward
694 approach (group-mean $b_0=4.15$; $t(26)=6.08$; $p<0.001$, Figure 2B), and an overweighting of reward
695 in the integration of value dimensions (group-mean $|b_1|-|b_2|=0.987$; $t(26)=3.59$; $p<0.001$, Figure
696 2B), consistent with previous studies (Shapiro and Grafton, 2020; Dundon et al., 2021; Pedersen
697 et al., 2021).

698

699

[Figure 2 here]

700

701 From these logistic models we classified each trial as offering either high or low conflict (see
702 methods). We confirmed that these classifications gave rise to the typical behavioral features of
703 encountering conflict: less consistent choice and lengthier RT. First, we observed in a
704 nonparametric estimate of choice consistency across participants, that there was a higher level
705 of deviation in choices (i.e., different choices registered at different times for similar offers,
706 enumerated with a bin-by-bin variance estimate (V); see methods) in trials identified as high
707 conflict ($V_{\text{choice,high}}=0.071$) compared to trials identified as low conflict ($V_{\text{choice,high}}=0$; $t(26)=13.23$,
708 $p<0.001$; Figure 2C). Next, we observed across participants in a comparison of median RT, that
709 responses were longer on trials identified as high conflict ($RT_{\text{high}}=2.02$ s) compared to trials
710 identified as low conflict ($RT_{\text{low}}=1.66$ s; $t(26)=12.10$, $p<0.001$; Figure 2C).

711

712 *Baseline computational model.* We next fitted a baseline hierarchical Bayesian drift-diffusion
713 model (HDDM; Wiecki et al., 2013), to get a clearer insight into how increased conflict alters the
714 computational parameters associated with choice and RT. This model (described in Eq. 6) fitted
715 distinct group-level DDM parameters $\{a,v,z,t\}$, depending on whether participants were making
716 choices on trials in states of low or high conflict. This baseline model revealed that in high conflict,
717 participants displayed a wider decision boundary (a), consistent with seeking more evidence
718 before executing their choices (Figure 2D; Table 2-1). The model also revealed that participants
719 reached this decision boundary by way of a dampened rate of evidence accumulation (v); Figure
720 2D; Table 2-1). Starting points (z) in this DDM also suggested an overall bias toward approach in
721 states of both low and high conflict, however this bias was attenuated in high conflict (Figure 2D;
722 Table 2-1). Finally, nonddecision time (t) was slightly shorter in high conflict (Figure 2D; Table 2-
723 1).

724

725 Summarizing the behavioral and baseline computational results so far, participants were reward
726 sensitive, but also confronted states of subjective "conflict". The parametric-behavioral response
727 to states of high conflict appeared to involve a larger requirement of evidence prior to committing
728 choices, a slower accumulation of evidence toward that criterion and an attenuated bias toward
729 approach behavior.

730

731 *Verifying neural symmetry's association with conflict.* Two within-subjects ANOVAs verified that
732 the SS_{sym} ($F(1,26)=8.29$, $p=0.008$) and α_{sym} ($F(1,26)=5.82$, $p=0.023$) "symmetry" traces varied
733 with conflict. For α , there was also an interaction with trial phase ($F(1,26)=11.9$, $p=0.002$): no
734 significant difference between conflict states early (mean difference=-0.008; $SE=0.012$;
735 $p_{Tukey}=0.906$), but higher symmetry in high conflict late (mean difference=-0.043; $SE=0.012$,
736 $p_{Tukey}=0.004$).

737

738

739 *Cross-modal (neural and cardiac-sympathetic) collaborative association with (DDM) parameters*

740 We next tested if DDM parameters were associated with trial-by-trial physiological fluctuations,
741 and if this association was unique to a specific state (i.e., low vs high conflict). Specifically, we
742 used an iterative modeling approach to find a best-fitting combination of physiological signals
743 associated with DDM parameters, with an emphasis on discovering cross-modal (i.e., neural and
744 cardiac) collaboration. We began this process with a total 17 candidate physiology signals. Neural
745 signals were: steady-state visually evoked potentials relevant for reward (SS_{rew}) and cost (SS_{shk})
746 information, in addition to the "symmetry" trace (SS_{sym}) enumerating the similarity between these

747 traces (i.e., the symmetry across the brain) over time (Figure 3A); spatially sensitive alpha power,
748 i.e., relevant for reward (α_{rew}) and cost (α_{shk}) information, in addition to a "symmetry" trace
749 (α_{sym}) enumerating their similarity over time (Figure 3B); frontal-midline theta power (theta)
750 and posterior-parietal delta (delta) power (Figure 3C). For each neural variable, we computed
751 average power in early ([0 s to 1 s] post offer onset) and late ([1 s to 2 s]) time windows, making
752 a total of 16 neural variables for each trial (Figure 3A–C). The 17th physiology signal was an
753 estimate of cardiac contractility (inotropy; Figure 3D). We averaged across a positively scored
754 contractility estimate for each heartbeat registered in the two-second window post offer onset
755 (Figure 3D).

756

757 *Singular models.* For the iterative modeling approach we first fitted a series of "singular" models
758 (Eq. 6) that probed whether modeling DDM parameters $\{a, v, z, t\}$ as a linear combination of a single
759 regressor (i.e., one trial-by-trial physiology signal) would provide a better-fitting model than the
760 baseline model described above. Using Deviance Information Criterion scores (DIC; Wiecki et al.,
761 2013) we observed that seven models provided an improved fit (Figure 3E); these models
762 respectively modeled the DDM parameters as a function of trial-by-trial fluctuations in late α_{sym}
763 ($-\Delta DIC=141.3$), late α_{shk} ($-\Delta DIC=129.8$), late α_{rew} ($-\Delta DIC=116.45$), contractility ($-\Delta DIC=39.6$),
764 early SS_{sym} ($-\Delta DIC=8.21$), late theta ($-\Delta DIC=5.54$) and early α_{rew} ($-\Delta DIC=2.31$).
765 A proxy for RT variance explained for the best fitting singular model is in Figure 3H. We therefore
766 established first that behavioral decompositions from the DDM were associated with both neural
767 and cardiac-sympathetic physiological signals that varied on a trial-by-trial basis, with neural
768 signals predominantly involving the alpha band, and signals measured in the later time window.

769

770

[Figure 3 here]

771

772 *Cross-modal models.* Singular models revealed associations between DDM parameters and both
773 neural and cardiac-sympathetic signals. We next fitted a series of "cross-modal" models (Eqs. 7–
774 8). These models tested if the singular models containing a neural regressor could be improved
775 by adding contractility as a second regressor (i.e., cross-modal). We restricted cross-modal
776 models to include neural variables from the singular models that were superior fits to baseline.
777 We also tested for evidence of both additive and interactive cross-modal collaboration. For
778 additive collaboration, we tested models with two regressors (the neural variable in question, and
779 contractility), while for interactive collaboration, we added a third interaction or "alignment"
780 regressor which was the normalized product of the neural variable in question and contractility.
781 This made 12 target cross-modal models in total (Figure 3F). We also updated the baseline, and
782 tested if these cross-modal models improved the fit relative to the best-fitting singular model, i.e.,
783 which had α_{sym} as its sole regressor (dashed line from Figure 3E to 3F). From resulting
784 differences in DIC scores, we observed six cross-modal models providing an improved fit over
785 baseline. All such models involved alpha-band activity recorded in the late window (Figure 3F).
786 The best-fitting model ($-\Delta\text{DIC}=29.0$) was additive; it contained α_{shk} , that is, alpha power
787 relevant for the cost information, alongside contractility, and no third alignment regressor. A proxy
788 for RT variance explained for the best fitting cross-modal model is in Figure 3H

789

790 *Complement models.* Our cross-modal models revealed that behavioral features could be
791 modeled by a neural variable relative to cost (α_{shk}) in addition to cardiac-sympathetic
792 fluctuations (contractility), i.e., side-by-side in the same model. However, given that cross-modal
793 models involving alpha power relevant to reward information (α_{rew}) and the symmetry of alpha
794 across the brain (α_{sym}) also provided improved fits (Figure 3F), we ran a final set of

795 "complement" models to test for their complementary association with DDM parameters (Eq. 9).
796 In other words, we tested if the outright best cross-modal fit (additive α_{shk} , marked "m1" in
797 Figure 3E) could be improved even further by also including complement (i.e., set difference)
798 parameters from either of the two best-fitting cross-modal models involving α_{rew} and α_{sym}
799 (each of which was interactive; each marked "m2" in Figure 3F). We again updated the baseline
800 to the best-fitting cross-modal model (dashed line from Figure 3F to 3G). From resulting
801 differences in DIC scores (Figure 3G), we observed both complement models to improve the fit,
802 with substantial improvement in the case of adding set difference parameters involving the
803 interactive cross-modal model with α_{sym} . ($-\Delta DIC=155.3$). In other words, the best-fitting
804 complement model modeled DDM parameters not just by α_{shk} and contractility, but also by
805 the symmetry of alpha across the brain (α_{sym}) and the product of α_{sym} and contractility. A
806 proxy for RT variance explained for the best fitting complement model is in Figure 3H. Our iterative
807 modeling approach therefore unearthed a set of both neural (exclusively alpha) and cardiac-
808 sympathetic physiological signals associated with parameters of the DDM, and further revealed
809 evidence for interactive cross-modal collaboration (i.e., neural and cardiac-sympathetic
810 alignment).

811
812 Inspecting the parameter posteriors of this best-fitting complement model (Figure 4A–D), the
813 majority of associations were with the decision boundary (a). Wider boundaries were
814 accompanied by a fairer spread of attention to all dimensions of available information, though this
815 was not exclusive to states of high conflict. In both low and high-conflict states, there was a
816 negative association between the boundary and alpha relevant to cost (α_{shk} ; Figure 4A; Table
817 4-1), suggesting greater desynchronization of alpha contralateral to cost information associated
818 with increased boundaries (consistent with more attention being allocated to that information).
819 Also in both conflict states, there were positive associations between the boundary and the

820 symmetry of alpha on either side of the brain (α_{sym} ; Figure 4A; Table 4-1). Widening
821 boundaries were therefore not solely associated with deploying attention to cost, but also a more
822 even spread of attention to both channels of information, consistent with a pursuit of greater
823 evidence, but in an additive, i.e., not overriding manner. The relationship between the boundary
824 and cardiac contractility was likewise observed in both states. This (positive) association was
825 consistent with wider boundaries also accompanying increased sympathetic drive (contractility;
826 Figure 4A; Table 4-1). Exclusive to states of high conflict, we identified the interactive aspect of
827 cross-modal collaboration, i.e., neural and cardiac-sympathetic signals aligning with meaningful
828 measures of behavior. That is, in addition to its linear relations with α_{sym} and contractility, the
829 boundary (as determined through the DDM) was additionally positively associated with their
830 alignment. Strikingly, this association only occurred in states of high conflict ($\alpha_{\text{sym}} * \text{cont.}$;
831 Figure 4A; Table 4-1). In other words, as participants made choices in high conflict, which was
832 linked with wider decision boundaries, part of this boundary widening was directly related to
833 alignment between a cardiac-sympathetic (positive inotropic) response and the degree of alpha
834 symmetry across the brain. This was the sole evidence of such interactive cross-modal
835 collaboration in our best-fitting model.

836
837 [Figure 4 here]

838
839 We observed more sparse associations between physiological signals and the remaining DDM
840 parameters. Drift rate (v) was not credibly associated with any signal (Figure 4B; Table 4-1). The
841 starting point (z) was related to alpha related to cost, only in states of high conflict (α_{shk} ; Figure
842 4C; Table 4-1). This positive association is consistent with a bias toward approach intensifying
843 when less attention is directed at the cost information (i.e., more synchronization of α_{shk}).

844 Finally, state-specific associations emerged relating to nondecision time (t). Nondecision time is
845 a constant term included in the DDM to account for early perceptual and motor preparation
846 processes. In low conflict, nondecision time was longer when alpha symmetry decreased, and
847 when alpha relevant to cost increased synchrony (α_{shk} and α_{sym} ; Figure 4D; Table 4-1).
848 Conversely, in high conflict, nondecision time was longer solely when α_{sym} increased (Figure
849 4D; Table 4-1).

850

851 To help clarify the underlying dynamics of the seeming three-way interaction and the decision
852 boundary (i.e., associations between the decision boundary and combinations of conflict, α_{sym}
853 and contractility) we fitted a modified version of the baseline model in Eq. 3. This model discretized
854 trials into eight bins depending on whether these three measures were high or low, and fitted a
855 separate decision boundary for each. Figure 4E and Table 4-2 respectively depict and
856 characterize the resulting parameter posteriors, expressed relative to a baseline (low conflict, low
857 late α_{sym} and low contractility). We here see that the decision boundary is credibly widest
858 when both contractility and the symmetry of alpha across the brain is high. This is consistent with
859 the interaction in Figure 4A being driven by the two signals synchronously increasing (i.e., higher
860 contractility alongside higher alpha symmetry) during moments of conflict.

861

862 We additionally fitted control models to assess whether cardiac-sympathetics might be a proxy
863 for more general activity levels in the brain, i.e., a global or frequency-specific increase in gain
864 (Figure 4F). In these models, we used the best-fitting complement model, substituting contractility
865 regressors (and interaction regressors featuring contractility) with an estimate of global field power
866 (GFP; Figure 4F) and total alpha power in the brain (whole brain alpha; Figure 4F). Only the model
867 substituting contractility with global field power (GFP) was a slightly better fit ($-\Delta DIC=5.78$).

868 However, inspecting parameters posteriors for the decision boundary in this control model
869 alongside the contractility complement model (right panels of Figure 4F; Table 4-2) we observed
870 a striking dissociation between the direction of associations. While the boundary is widest for high
871 levels of contractility and α_{sym} , alignment of GFP and late α_{sym} was instead associated
872 with smaller boundaries (parameters marked with arrows in figure 4F). This strengthens the case
873 that contractility might be part of a physiological response to scrutinize evidence in a conflicting
874 situation, in contrast to other brain signals that might instead be associated with an urgency to
875 respond more quickly.

876
877 *Inter-trial alpha-phase coherence.* In the above section we observed that alpha dynamics and
878 their alignment with cardiac-sympathetic signals were associated with behavioral parameters
879 during the approach-avoidance conflict. That is, during high-conflict choices, the width of the
880 decision boundary was positively associated with the alignment between contractility and alpha
881 symmetry. We lastly sought additional evidence (outside of computational models) regarding the
882 nature and characteristics of the relationship between contractility and alpha dynamics. For this,
883 we probed how the state of cardiac-sympathetics (specifically, whether contractility was high or
884 low) was associated with coherence of alpha power across trials, separately for alpha power
885 relevant to both the reward and cost information, and separately again for high and low-conflict
886 trials. We extracted the phase angle of these waveforms over time, i.e., $\alpha_{\text{rew}}\theta$ and $\alpha_{\text{shk}}\theta$.
887 Figure 4G depicts $\alpha_{\text{rew}}\theta$ and $\alpha_{\text{shk}}\theta$ summarized across trials and participants, separately
888 for trials that were above (high contractility) or below (low contractility) a participant's median.
889 Note that the waveforms in Figure 4 only show trials in states of high conflict. Here we observe
890 alpha-like oscillations present in each time series, indicating coherence across trials. However,
891 during the later time window, the sinusoidal patterning in $\alpha_{\text{rew}}\theta$ (Figure 4G top panel) appears
892 to be greater on low-tractility trials. A three-way within-subjects ANOVA of summarized

893 rectified phase angles $|\theta|$ as a function of the timeseries ($\alpha_{rew}\theta$, $\alpha_{shk}\theta$), time window (early,
894 late) and contractility (high, low) confirmed by way of a three-way interaction ($F(1,26)=5.84$,
895 $p=0.023$) that coherence was indeed higher in low contractility ($|\theta|=0.117$) vs high contractility
896 ($|\theta|=0.091$; $p_{Tukey}=0.012$), only in the $\alpha_{rew}\theta$ timeseries and only in the late time window (Figure
897 4H). In addition, the same three-way ANOVA returned no three-way interaction for trials in states
898 of low conflict ($F(1,26)=0.5033$, $p=0.484$). Thus, this additional analysis using both raw data and
899 an alternative means to look at frequency decomposition (coherence vs power) first supports the
900 idea that the relationship between contractility and alpha dynamics is relevant primarily in states
901 of high conflict. In addition, the reduced coherence across trials in alpha power relevant for reward
902 when contractility was high, uniquely observed for high-conflict trials, additionally reveals a
903 potential mechanistic role of for the sympathetic response during conflict. That is, fair assessment
904 of all available information during a high-conflict decision might require disrupting a dominant
905 reward-related signal, and sympathetic systems might contribute to this disruption.

906

907

908 Discussion

909

910 Event-related physiological sciences have laid the foundations to explore cross-modal (i.e., neural
911 and cardiac-sympathetic) collaboration subserving complex value-based behavior. We recorded
912 parallel continuous electroencephalographic and cardiac-sympathetic data to probe associations
913 between cognitive-neural and cardiac-sympathetic responses (contractility) while humans
914 performed a modified version of the approach-avoidance paradigm. Our findings suggest
915 participants were reward sensitive but encountered "conflict" when approach and avoidance
916 presented similar value. Using the drift-diffusion model (DDM), we computationally decomposed

917 their behavior during conflict, which principally involved a widened decision boundary, consistent
918 with pursuit of more evidence prior to choices. Our best-fitting model of DDM dynamics suggested
919 that regardless of the state (low or high conflict), the boundary increased alongside increased
920 goal-directed attention to both costs and rewards, as well as alongside increased cardiac
921 contractility. However, exclusively in states of high conflict, the alignment of neural and cardiac-
922 sympathetic was associated with additional increase of the boundary width. This association was
923 markedly different from those involving alternative proxy measures of neural gain. Together, these
924 findings offer the first evidence of a potential interactive cross-modal collaboration of neural and
925 cardiac-sympathetic systems during evidence scrutiny in conflicting value-based decisions.
926 Analyses involving cross-trial coherence additionally proposed a putative role for sympathetics,
927 i.e., disrupting the dominance of reward signals.

928
929 Our findings suggest that cardiac-sympathetic activity is closely linked with neural processes and
930 specific behavioral parameters during approach-avoidance conflict, indicating that these
931 peripheral responses may be recruited by cognitive processes. Beginning with cardiac-
932 sympathetics, the contractility-boundary relations are broadly consistent with sympathetic
933 reactivity in contexts of increasing uncertainty (Palacios-Filardo and Mellor, 2019) and greater
934 difficulty (Richter et al., 2008). However, our cross-trial coherence findings are the strongest
935 evidence yet that the drivers of sympathetic reactivity might influence dominant reward-signal
936 processing during value-based conflict. Under a value-based framework, such a role would not
937 necessarily conflict with other previous findings associating cardiac indices with the pursuit of
938 reward (Richter et al., 2016). That is, a uniform behavioral policy (i.e., approaching all or avoiding
939 all) for offers presenting high conflict will result in long-term net-negative yields (either from
940 mounting incremental costs incurred or mounting incremental opportunity reward costs
941 eschewed). Optimal behavior should instead try as best as possible to map an efficiently

942 enumerated net value (i.e., positive or negative subjective value) onto the appropriate action.
943 Across decision-making contexts, humans are usually biased toward more desirable information
944 (Sharot and Garrett, 2016), to the extent that an insensitivity to reward has been reported as a
945 robust computational phenotype of psychiatric conditions such as depression (Garrett et al., 2014;
946 Pedersen et al., 2021). In the present study, and in at least two separately reported human studies
947 using the same task settings (Volz et al., 2017; Shapiro and Grafton 2020), participants
948 consistently overweighted reward when making choices. More recent evidence using transiently
949 disruptive cortical stimulation further proposes that reward sensitivity might not simply reflect
950 impulsivity, but a cortically-mediated model of a person's primary goal in a value-based setting
951 (i.e., capture reward; Rolle et al., 2022). Integrating these findings with our findings under the
952 above value-based framework, it might therefore be physiologically efficient to prioritize reward
953 information, and reserve effortful scrutiny and juxtaposition involving multiple streams of
954 information for moments of conflict. Reward sensitivity also generalizes to dynamic learning tasks,
955 where recent studies report that people learn faster from positive-vs-negative prediction errors
956 (Lefebvre et al., 2017; Garrett and Daw, 2020; Dundon et al., 2020). Consistent with our present
957 findings, this learning asymmetry attenuates (i.e., learning from negative outcomes occurs more
958 rapidly) when sympathetic activity is elevated (Garrett et al., 2018; Dundon et al., 2020), to the
959 extent that sympathetic reactivity even predicts individual participants who adjust their behavior
960 more optimally to declining changes in their environment (Dundon et al., 2020). Whether the
961 neural sources for cardiac-sympathetics serve common mechanisms to resolve uncertainty and
962 address biases across decisions and learning is an exciting avenue of future research.

963

964 We additionally observed a collaborative association involving neural dynamics in the alpha band.
965 Broadly considered to reflect inhibition (Jensen and Mazaheri, 2010) and visual spatial attention
966 (Worden et al., 2000), alpha power also shows a correspondingly flexible and goal-directed profile

967 in cognitive processing. For example, during spatial recall, alpha power can code spatial targets
968 in the absence of external information (MacLean et al, 2019) consistent with post-perceptual goal
969 maintenance. If participants are cued to switch recall to a different memory location after memory
970 arrays disappear, alpha dynamics can likewise switch from encoding the initial target to encoding
971 the new one (van Moorselaar et al., 2018). Alpha power can additionally signal a person's
972 willingness to take future risks (Zhang et al., 2018), suggesting it also responds in more value-
973 based settings. Together, these findings are consistent with our interpretation that late alpha
974 power mediated "fair assessment", i.e., a shift in attention to process additional (cost) information
975 alongside the reward signal information. Interestingly, we observed less association between
976 steady-state visually-evoked potentials (SS) and DDM parameters. This might be due to task
977 requirements. Earlier work implicates SS in coding information relevant for DDM decision
978 boundaries (O'Connell et al, 2012), albeit in tasks requiring perceptual and not value-based
979 decisions. Our task used large visually unambiguous stimuli and created conflict that was value-
980 based (subjective) rather than perceptually driven. Recent human (Zhigalov and Jensen, 2020)
981 and nonhuman (Bastos et al., 2020) work dissociates alpha signals from modulating gain of
982 sensory information, consistent with the idea that these signals have greater relevance for
983 behavioral responses in value-based settings. Our paradigm modifications might also explain the
984 associations we observed principally involving visual attention (alpha) signals over those
985 associated with cognitive control (theta) and decision making (delta). Given the varied possible
986 sites of cortical control for the sympathetics (Dum et al., 2019), future work should not disregard
987 any potential association between these latter signals and sympathetics, and perhaps modify the
988 approach-avoidance paradigm to exploit them more selectively.

989

990 We lastly speculate on a network of substrates that might underly behaviorally relevant interaction
991 between the neural (alpha) and cardiac-sympathetic (contractility) signals in states of high conflict.

992 It is highly likely that our observed neural dynamics in the alpha band were facilitated by
993 noradrenergic (NE) projections from the locus coeruleus in the brainstem (LC; Rajkowski, 1993;
994 Aston-Jones and Cohen, 2005; Joshi and Gold, 2020). The LC-NE system innervates cortical
995 areas involved in orienting attention (e.g., parietal; Foote and Morrison, 1987), responding to
996 arousal (Sara and Bouret, 2012), goal-relevant stimuli, and exploration (Aston-Jones and Cohen,
997 2005), all of which are likely relevant during moments of conflict. LC-NE can also broadly influence
998 sympathetic activity (Samuels and Szabadi, 2008b). However, when it comes specifically to
999 cardiac activity, evidence from both animal-optogenetic (Wang et al., 2014) and human-imaging
1000 (Wood et al., 2017) studies suggest LC-NE influences heart rate via vagal (i.e., parasympathetic)
1001 channels, contrasting with our specific cardiac assay—contractility (inotropy)—which primarily
1002 tracks beta-adrenergic sympathetic drive to the heart (see discussion in Stump et al., 2023; also
1003 see methods for how, in our study, we corrected for influences of heart rate and respiratory cycle).
1004 A key subcortical controller of this cardiac-sympathetic response is the rostral ventrolateral
1005 medulla in the brainstem (RVLM; Mandal et al., 1990; Shapoval et al., 1991; Kulkarni et al., 2023),
1006 which is the primary source of organ-specific sympathetic preganglionic neurons. RVLM
1007 principally receives inputs from the cortically modulated hypothalamus (Dum et al., 2019; Kono et
1008 al., 2020; Koba et al., 2022). LC has few direct efferent connections with RVLM, although it might
1009 communicate indirectly via its projections to the paraventricular nucleus of the hypothalamus. The
1010 behavioral changes we observed when neural (alpha) and cardiac-sympathetic (contractility)
1011 signals interact may therefore reflect two subcortical nodes (LC-NE and RVLM) activating
1012 concurrently. Alternatively, alpha-contractility associated collaboration may ultimately be
1013 mediated by interactions at the cortical level.

1014

1015 It is important to note that while our current data offer an important step toward resolving whether
1016 complex cognition actively recruits peripheral responses, our findings are correlational, and

1017 should not be taken as evidence of direct mechanistic causality. Future studies incorporating
1018 selective modulation of peripheral responses, such as cardiac-specific pharmacological
1019 interventions, could further probe the causality and directionality of these interactions. Future
1020 studies should also aim to clarify the role of peripheral responses alongside brain functions not
1021 examined here, particularly subcortical activity and alternative measures of gain. In addition, while
1022 the DDM provides an elegant and intuitive decomposition of decision behavior, it remains a
1023 hypothesis of underlying mechanistic function and can potentially carry the risk of over-
1024 parameterization (Ratcliff et al., 2016). A more direct paradigm will be needed to replicate and
1025 validate our mechanistic interpretations.

1026

1027 *Concluding remarks*

1028 We reveal that fair assessment of all available information (i.e., not just rewards) during a high-
1029 conflict decision potentially requires orchestration of both cognitive mechanisms and sympathetic
1030 activity. In terms of clinical relevance, autonomic function is vulnerable to neurodegenerative
1031 conditions such as Alzheimer's and Parkinson's disease (Samuels and Szabadi, 2008b;
1032 Engelender and Isacson, 2017). Future research may therefore test if features of cross-modal
1033 collaboration during complex cognition can assist with early detection.

1034

1035

1036 **Acknowledgements**

1037

1038 Acknowledgments: The research was supported by award W911NF-16-1-0474 from the Army
1039 Research Office and by the Institute for Collaborative Biotechnologies under Cooperative
1040 Agreement W911NF-19-2-0026 with the Army Research Office.

1041

1042

1043 **Author contributions**

1044 Designed research: NMD, STG, JOG

1045 Performed research: AS

1046 Contributed analytic tools: AS, TB, VB, ER, DY, BG

1047 Analyzed data: NMD

1048 Wrote the paper: NMD, AS, TB, JOG, VB, ER, DY, BG, STG

1049

1050

1051 **References**

1052

1053 Amemori, K. I., & Graybiel, A. M. (2012). Localized microstimulation of primate pregenual
1054 cingulate cortex induces negative decision-making. *Nature Neuroscience*, *15*(5), 776–785.

1055

1056 Amemori, K. I., Amemori, S., & Graybiel, A. M. (2015). Motivation and affective judgments
1057 differentially recruit neurons in the primate dorsolateral prefrontal and anterior cingulate
1058 cortex. *Journal of Neuroscience*, *35*(5), 1939–1953.

1059
1060
1061
1062
1063
1064
1065
1066
1067
1068
1069
1070
1071
1072
1073
1074
1075
1076
1077
1078
1079

Aston-Jones, G., & Cohen, J. D. (2005). An integrative theory of locus coeruleus-norepinephrine function: adaptive gain and optimal performance. *Annual Review of Neuroscience*, 28, 403–450.

Ballard, I. C., & McClure, S. M. (2019). Joint modeling of reaction times and choice improves parameter identifiability in reinforcement learning models. *Journal of Neuroscience Methods*, 317, 37–44.

Bastos, A. M., Lundqvist, M., Waite, A. S., Kopell, N., & Miller, E. K. (2020). Layer and rhythm specificity for predictive routing. *Proceedings of the National Academy of Sciences*, 117(49), 31459–31469.

Bottemanne, L., & Dreher, J. C. (2019). Vicarious rewards modulate the drift rate of evidence accumulation from the drift diffusion model. *Frontiers in Behavioral Neuroscience*, 13, 142.

Brainard, D. H. (1997). The Psychophysics Toolbox. *Spatial Vision*, 10(4), 433–436.

Callister, R., Suwarno, N. O., & Seals, D. R. (1992). Sympathetic activity is influenced by task difficulty and stress perception during mental challenge in humans. *The Journal of Physiology*, 454(1), 373–387.

1080 Champion, R. A. (1961). Motivational effects in approach-avoidance conflict. *Psychological*
1081 *Review*, 68(5), 354.

1082

1083 Cieslak, M., Ryan, W. S., Babenko, V., Erro, H., Rathbun, Z. M., Meiring, W., ... & Grafton, S. T.
1084 (2018). Quantifying rapid changes in cardiovascular state with a moving ensemble
1085 average. *Psychophysiology*, 55(4), e13018.

1086

1087 Colas, J. T. (2017). Value-based decision making via sequential sampling with hierarchical
1088 competition and attentional modulation. *PloS one*, 12(10), e0186822.

1089

1090 Delorme, A., & Makeig, S. (2004). EEGLAB: An open source toolbox for analysis of single-trial
1091 EEG dynamics including independent component analysis. *Journal of Neuroscience*
1092 *Methods*, 134(1), 9–21.

1093

1094 Dum, R. P., Levinthal, D. J., & Strick, P. L. (2019). The mind-body problem: Circuits that link the
1095 cerebral cortex to the adrenal medulla. *Proceedings of the National Academy of*
1096 *Sciences*, 116(52), 26321–26328.

1097

1098 Dundon, N. M., Colas, J. T., Garrett, N., Babenko, V., Rizer, E., Yang, D., ... & Grafton, S. T.
1099 (2023). Decision heuristics in contexts integrating action selection and execution. *Scientific*
1100 *Reports*, 13(1), 6486.

1101

1102 Dundon, N. M., Garrett, N., Babenko, V., Cieslak, M., Daw, N. D., & Grafton, S. T. (2020).
1103 Sympathetic involvement in time-constrained sequential foraging. *Cognitive, Affective, &*
1104 *Behavioral Neuroscience*, *20*, 730–745.

1105

1106 Dundon, N. M., Shapiro, A. D., Babenko, V., Okafor, G. N., & Grafton, S. T. (2021).
1107 Ventromedial prefrontal cortex activity and sympathetic allostasis during value-based
1108 ambivalence. *Frontiers in Behavioral Neuroscience*, *15*, 615796.

1109

1110 Elliot, A. J., & Thrash, T. M. (2002). Approach-avoidance motivation in personality: Approach
1111 and avoidance temperaments and goals. *Journal of Personality and Social Psychology*, *82*(5),
1112 804.

1113

1114 Engelender, S., & Isacson, O. (2017). The threshold theory for Parkinson's disease. *Trends in*
1115 *Neurosciences*, *40*(1), 4–14.

1116

1117 Fontanesi, L., Gluth, S., Spektor, M. S., & Rieskamp, J. (2019). A reinforcement learning
1118 diffusion decision model for value-based decisions. *Psychonomic Bulletin & Review*, *26*(4),
1119 1099–1121.

1120

1121 Foote, S. L., & Morrison, J. H. (1987). Extrathalamic modulation of cortical function. *Annual*
1122 *Review of Neuroscience*, *10*(1), 67–95.

1123

1124 Forstmann, B. U., Ratcliff, R., & Wagenmakers, E. J. (2016). Sequential sampling models in
1125 cognitive neuroscience: Advantages, applications, and extensions. *Annual Review of*
1126 *Psychology*, 67, 641–666.

1127

1128 Foxe, J. J., & Snyder, A. C. (2011). The role of alpha-band brain oscillations as a sensory
1129 suppression mechanism during selective attention. *Frontiers in Psychology*, 2, 154.

1130

1131 Frank, M. J., Gagne, C., Nyhus, E., Masters, S., Wiecki, T. V., Cavanagh, J. F., & Badre, D.
1132 (2015). fMRI and EEG predictors of dynamic decision parameters during human reinforcement
1133 learning. *Journal of Neuroscience*, 35(2), 485–494.

1134

1135 Galloway, N. R. (1990). Human brain electrophysiology: Evoked potentials and evoked
1136 magnetic fields in science and medicine. *The British Journal of Ophthalmology*, 74(4), 255.

1137

1138 Garrett, N., & Daw, N. D. (2020). Biased belief updating and suboptimal choice in foraging
1139 decisions. *Nature Communications*, 11(1), 3417.

1140

1141 Garrett, N., González-Garzón, A. M., Foulkes, L., Levita, L., & Sharot, T. (2018). Updating
1142 beliefs under perceived threat. *Journal of Neuroscience*, 38(36), 7901–7911.

1143

1144 Garrett, N., Sharot, T., Faulkner, P., Korn, C. W., Roiser, J. P., & Dolan, R. J. (2014). Losing the
1145 rose tinted glasses: Neural substrates of unbiased belief updating in depression. *Frontiers in*
1146 *Human Neuroscience*, 8, 639.

1147

1148 Gulbinaite, R., Rooszendaal, D. H., & VanRullen, R. (2019). Attention differentially modulates the
1149 amplitude of resonance frequencies in the visual cortex. *NeuroImage*, 203, 116146.

1150

1151 Gupta, A., Bansal, R., Alashwal, H., Kacar, A. S., Balci, F., & Moustafa, A. A. (2022). Neural
1152 substrates of the drift-diffusion model in brain disorders. *Frontiers in Computational*
1153 *Neuroscience*, 15, 678232.

1154

1155 Harper, J., Malone, S. M., & Bernat, E. M. (2014). Theta and delta band activity explain N2 and
1156 P3 ERP component activity in a go/no-go task. *Clinical Neurophysiology*, 125(1), 124–132.

1157

1158 Jensen, O., & Mazaheri, A. (2010). Shaping functional architecture by oscillatory alpha activity:
1159 gating by inhibition. *Frontiers in Human Neuroscience*, 4, 186.

1160

1161 Joshi, S., & Gold, J. I. (2020). Pupil size as a window on neural substrates of cognition. *Trends*
1162 *in Cognitive Sciences*, 24(6), 466–480.

1163

1164 Kleiner, M., Brainard, D., & Pelli, D. (2007). What's new in Psychtoolbox-3? *Perception* 36
1165 *ECVP Abstract Supplement*.

1166

1167 Klimesch, W. (2012). Alpha-band oscillations, attention, and controlled access to stored
1168 information. *Trends in Cognitive Sciences*, 16(12), 606–617.

1169

1170 Koba, S., Kumada, N., Narai, E., Kataoka, N., Nakamura, K., & Watanabe, T. (2022). A
1171 brainstem monosynaptic excitatory pathway that drives locomotor activities and sympathetic
1172 cardiovascular responses. *Nature Communications*, 13(1), 5079.

1173

1174 Kono, Y., Yokota, S., Fukushi, I., Arima, Y., Onimaru, H., Okazaki, S., ... & Okada, Y. (2020).
1175 Structural and functional connectivity from the dorsomedial hypothalamus to the ventral medulla
1176 as a chronological amplifier of sympathetic outflow. *Scientific Reports*, 10(1), 13325.

1177

1178 Kothe, C. A., & Makeig, S. (2013). BCILAB: A platform for brain-computer interface
1179 development. *Journal of Neural Engineering*, 10(5), 056014.

1180

1181 Kulkarni, S. S., Mischel, N. A., & Mueller, P. J. (2023). Revisiting differential control of
1182 sympathetic outflow by the rostral ventrolateral medulla. *Frontiers in Physiology*, 13, 2761.

1183

1184 Lefebvre, G., Lebreton, M., Meyniel, F., Bourgeois-Gironde, S., & Palminteri, S. (2017).
1185 Behavioural and neural characterization of optimistic reinforcement learning. *Nature Human*
1186 *Behaviour*, 1(4), 0067.

1187

1188 Lewis, R. P., Leighton, R. F., Forester, W. F., & Weissler, A. M. (1974). Systolic time intervals.
1189 In A. M. Weissler (Ed.), *Noninvasive cardiology* (pp. 301–368). Grune and Stratton.

1190

1191 Light, K. C. (1985). Cardiovascular and renal responses to competitive mental challenges. In J.
1192 F. Orlebeke, G. Mulder, & L. J. P. van Doornen (Eds.), *Cardiovascular psychophysiology:
1193 Theory and methods* (pp. 683–702). Plenum.

1194

1195 Linden, W. (1985). Cardiovascular response as a function of predisposition, coping behavior
1196 and stimulus type. *Journal of Psychosomatic Research*, 29(6), 611–620.

1197

1198 Luu, P., Tucker, D. M., & Makeig, S. (2004). Frontal midline
1199 and the error-related negativity: Neurophysiological mechanisms of action regulation. *Clinical
1200 Neurophysiology*, 115(8), 1821–1835.

1201

1202 MacLean, M. H., Bullock, T., & Giesbrecht, B. (2019). Dual process coding of recalled locations
1203 in human oscillatory brain activity. *Journal of Neuroscience*, 39(34), 6737–6750.

1204

1205 Mandal, A. K., Kellar, K. J., Norman, W. P., & Gillis, R. A. (1990). Stimulation of serotonin₂
1206 receptors in the ventrolateral medulla of the cat results in nonuniform increases in sympathetic
1207 outflow. *Circulation Research*, 67(5), 1267–1280.

1208

1209 McLoughlin, G., Palmer, J. A., Rijdsdijk, F., & Makeig, S. (2014). Genetic overlap between
1210 evoked frontocentral theta-band phase variability, reaction time variability, and attention-
1211 deficit/hyperactivity disorder symptoms in a twin study. *Biological Psychiatry*, 75(3), 238–247.

1212

1213 Mullen T. (2012). *NITRC: CleanLine: Tool/Resource Info*. <http://www.nitrc.org/projects/cleanline>

1214

1215 Müller, M. M., Andersen, S., Trujillo, N. J., Valdes-Sosa, P., Malinowski, P., & Hillyard, S.
1216 (2006). Feature-selective attention enhances color signals in early visual areas of the human
1217 brain. *Proceedings of the National Academy of Sciences*, 103(38), 14250–14254.

1218

1219 Müller, M. M., Picton, T. W., Valdes-Sosa, P., Riera, J., Teder-Sälejärvi, W. A., & Hillyard, S. A.
1220 (1998). Effects of spatial selective attention on the steady-state visual evoked potential in the
1221 20–28 Hz range. *Cognitive Brain Research*, 6(4), 249–261.

1222

1223 Navarro, D. J., & Fuss, I. G. (2009). Fast and accurate calculations for first-passage times in
1224 Wiener diffusion models. *Journal of Mathematical Psychology*, 53(4), 222–230.

1225

1226 Newlin, D. B., & Levenson, R. W. (1979). Pre-ejection period: Measuring beta-adrenergic
1227 influences upon the heart. *Psychophysiology*, 16(6), 546–552.

1228

1229 O'Connell, R. G., Dockree, P. M., & Kelly, S. P. (2012). A supramodal accumulation-to-bound
1230 signal that determines perceptual decisions in humans. *Nature Neuroscience*, *15*(12), 1729–
1231 1735.

1232

1233 O'Connell, R. G., Shadlen, M. N., Wong-Lin, K., & Kelly, S. P. (2018). Bridging neural and
1234 computational viewpoints on perceptual decision-making. *Trends in Neurosciences*, *41*(11),
1235 838–852.

1236

1237 Ogden, R. S., Henderson, J., McGlone, F., & Richter, M. (2019). Time distortion under threat:
1238 Sympathetic arousal predicts time distortion only in the context of negative, highly arousing
1239 stimuli. *PLoS one*, *14*(5), e0216704

1240

1241 Palacios-Filardo, J., & Mellor, J. R. (2019). Neuromodulation of hippocampal long-term synaptic
1242 plasticity. *Current Opinion in Neurobiology*, *54*, 37–43.

1243

1244 Pedersen, M. L., Ironside, M., Amemori, K. I., McGrath, C. L., Kang, M. S., Graybiel, A. M., ... &
1245 Frank, M. J. (2021). Computational phenotyping of brain-behavior dynamics underlying
1246 approach-avoidance conflict in major depressive disorder. *PLoS Computational Biology*, *17*(5),
1247 e1008955.

1248

1249 Pelli, D. G. (1997). The VideoToolbox software for visual psychophysics: Transforming numbers
1250 into movies. *Spatial Vision*, *10*, 437–442.

1251
1252 Peters, J., & D'Esposito, M. (2020). The drift diffusion model as the choice rule in inter-temporal
1253 and risky choice: A case study in medial orbitofrontal cortex lesion patients and controls. *PLoS*
1254 *Computational Biology*, 16(4), e1007615.

1255
1256 Pfurtscheller G, & Aranibar A. (1977). Event-related cortical desynchronization detected by
1257 power measurements of scalp EEG. *Electroencephalography and Clinical Neurophysiology*,
1258 42(6), 817–26.

1259
1260 Pion-Tonachini, L., Kreutz-Delgado, K., & Makeig, S. (2019). ICLabel: An automated
1261 electroencephalographic independent component classifier, dataset, and website.
1262 *NeuroImage*, 198, 181–197.

1263
1264 Rajkowski, J., Kubiak, P., & Aston-Jones, G. (1993). Correlations between locus coeruleus (LC)
1265 neural activity, pupil diameter and behavior in monkey support a role of LC in attention. *Society*
1266 *for Neuroscience Abstracts*, 19(1–3), 974.

1267
1268 Ratcliff, R., & McKoon, G. (2008). The diffusion decision model: Theory and data for two-choice
1269 decision tasks. *Neural Computation*, 20(4), 873–922.

1270

1271 Ratcliff, R., & Frank, M. J. (2012). Reinforcement-based decision making in corticostriatal
1272 circuits: mutual constraints by neurocomputational and diffusion models. *Neural*
1273 *Computation*, 24(5), 1186–1229.

1274

1275 Ratcliff, R., Smith, P. L., Brown, S. D., & McKoon, G. (2016). Diffusion decision model: Current
1276 issues and history. *Trends in cognitive sciences*, 20(4), 260-281.

1277

1278 Richter, M., Friedrich, A., & Gendolla, G. H. (2008). Task difficulty effects on cardiac
1279 activity. *Psychophysiology*, 45(5), 869–875.

1280

1281 Richter, M., Gendolla, G. H. E., & Wright, R. A. (2016). Three decades of research on
1282 motivational intensity theory: What we have learned about effort and what we still don't
1283 know. *Advances in Motivation Science*, 3, 149–186.

1284

1285 Rolle, C. E., Pedersen, M. L., Johnson, N., Amemori, K. I., Ironside, M., Graybiel, A. M., ... &
1286 Etkin, A. (2022). The role of the dorsal-lateral prefrontal cortex in reward sensitivity during
1287 approach-avoidance conflict. *Cerebral Cortex*, 32(6), 1269–1285.

1288

1289 Salvatier, J., Wiecki, T. V., & Fonnesebeck, C. (2016). Probabilistic programming in Python using
1290 PyMC3. *PeerJ Computer Science*, 2, e55.

1291

1292 Samuels, E. R., & Szabadi, E. (2008a). Functional neuroanatomy of the noradrenergic locus
1293 coeruleus: its roles in the regulation of arousal and autonomic function part I: Principles of
1294 functional organisation. *Current Neuropharmacology*, 6(3), 235–253.

1295

1296 Samuels, E. R., & Szabadi, E. R. S. A. E. (2008b). Functional neuroanatomy of the
1297 noradrenergic locus coeruleus: Its roles in the regulation of arousal and autonomic function part
1298 II: physiological and pharmacological manipulations and pathological alterations of locus
1299 coeruleus activity in humans. *Current Neuropharmacology*, 6(3), 254–285.

1300

1301 Sara, S. J., & Bouret, S. (2012). Orienting and reorienting: the locus coeruleus mediates
1302 cognition through arousal. *Neuron*, 76(1), 130–141.

1303

1304 Shahar, N., Hauser, T. U., Moutoussis, M., Moran, R., Keramati, M., Nspn Consortium, & Dolan,
1305 R. J. (2019). Improving the reliability of model-based decision-making estimates in the two-
1306 stage decision task with reaction-times and drift-diffusion modeling. *PLoS Computational*
1307 *Biology*, 15(2), e1006803.

1308

1309 Shapiro, A. D., & Grafton, S. T. (2020). Subjective value then confidence in human ventromedial
1310 prefrontal cortex. *Plos One*, 15(2), e0225617.

1311

1312 Shapoval, L. N., Sagach, V. F., & Pobegailo, L. S. (1991). Chemosensitive ventrolateral medulla
1313 in the cat: the fine structure and GABA-induced cardiovascular effects. *Journal of the Autonomic*
1314 *Nervous System*, 36(3), 159–172.

1315

1316 Sharot, T., & Garrett, N. (2016). Forming beliefs: Why valence matters. *Trends in Cognitive*
1317 *Sciences*, 20(1), 25–33.

1318

1319 Sherwood, A., Allen, M. T., Fahrenberg, J., Kelsey, R. M., Lovallo, W. R., & Van Doornen, L. J.
1320 (1990). Methodological guidelines for impedance cardiography. *Psychophysiology*, 27(1), 1–23.

1321

1322 Sherwood, A., Allen, M. T., Obrist, P. A., & Langer, A. W. (1986). Evaluation of beta-adrenergic
1323 influences on cardiovascular and metabolic adjustments to physical and psychological
1324 stress. *Psychophysiology*, 23(1), 89–104.

1325

1326 Skrandies, W. (1990). Global field power and topographic similarity. *Brain topography*, 3, 137–
1327 141.

1328

1329 Stump, A., Gregory, C., Babenko, V., Rizor, E., Bullock, T., Macy, A., Giesbrecht, B., Grafton, S.
1330 T., & Dundon, N. M. (2023). Non-invasive monitoring of cardiac contractility: Trans-radial
1331 electrical bioimpedance velocimetry (TREV). *Psychophysiology*, 00, e14411.

1332

1333 Usher, M., & McClelland, J. L. (2001). The time course of perceptual choice: The leaky,
1334 competing accumulator model. *Psychological Review*, 108(3), 550.

1335

1336 van Moorselaar, D., Foster, J. J., Sutterer, D. W., Theeuwes, J., Olivers, C. N., & Awh, E.
1337 (2018). Spatially selective alpha oscillations reveal moment-by-moment trade-offs between
1338 working memory and attention. *Journal of Cognitive Neuroscience*, 30(2), 256–266

1339

1340 Volz, L. J., Welborn, B. L., Gobel, M. S., Gazzaniga, M. S., & Grafton, S. T. (2017). Harm to self
1341 outweighs benefit to others in moral decision making. *Proceedings of the National Academy of
1342 Sciences*, 114(30), 7963–7968.

1343

1344 Wang, C., Rajagovindan, R., Han, S. M., & Ding, M. (2016). Top-down control of visual alpha
1345 oscillations: Sources of control signals and their mechanisms of action. *Frontiers in Human
1346 Neuroscience*, 10, 15.

1347

1348 Wang, X., Piñol, R. A., Byrne, P., & Mendelowitz, D. (2014). Optogenetic stimulation of locus
1349 ceruleus neurons augments inhibitory transmission to parasympathetic cardiac vagal neurons
1350 via activation of brainstem $\alpha 1$ and $\beta 1$ receptors. *Journal of Neuroscience*, 34(18), 6182–6189.

1351

1352 Wiecki, T. V., Sofer, I., & Frank, M. J. (2013). HDDM: Hierarchical Bayesian estimation of the
1353 drift-diffusion model in Python. *Frontiers in Neuroinformatics*, 7(14), 1–10.

1354

1355 Wood, C. S., Valentino, R. J., & Wood, S. K. (2017). Individual differences in the locus
1356 coeruleus-norepinephrine system: Relevance to stress-induced cardiovascular vulnerability.
1357 *Physiology & Behavior*, 172, 40–48.

1358

1359 Worden, M. S., Foxe, J. J., Wang, N., & Simpson, G. V. (2000). Anticipatory biasing of
1360 visuospatial attention indexed by retinotopically specific alpha-band electroencephalography
1361 increases over occipital cortex. *The Journal of Neuroscience: The Official Journal of the Society
1362 for Neuroscience*, 20(6), RC63–RC63.

1363

1364 Zhang, D., & Gu, R. (2018). Behavioral preference in sequential decision-making and its
1365 association with anxiety. *Human Brain Mapping*, 39(6), 2482–2499.

1366

1367 Zhigalov, A., & Jensen, O. (2020). Alpha oscillations do not implement gain control in early
1368 visual cortex but rather gating in parieto-occipital regions. *Human Brain Mapping*, 41(18), 5176–
1369 5186.

1370
1371
1372

1373 **Figure 1 Approach-avoidance and drift-diffusion model frameworks**

1374 (A) In the approach-avoidance paradigm participants integrate a reward and a cost in a "take-
1375 both-or-leave-both" choice regarding a compound offer. Varying the levels of reward and cost
1376 over multiple offers affords a two-dimensional logistic framework that can identify subjective value

1377 (p(approach); red-green gradient) and "conflict" (aqua-fuchsia gradient) across the decision
1378 space. Conflict is maximal near a "threshold" (dashed line), i.e., as p(approach) nears 0.50. Four
1379 example offers are shown (a–d) that vary in subjective value and conflict.

1380

1381 (B) High conflict (fuchsia) typically makes choices less consistent with lengthier RT.

1382

1383 (C) The slope of the "threshold" characterizes a sensitivity for reward or cost. Fitting the logistic
1384 model separately for each participant accounts for such sensitivities prior to enumerating where
1385 in decision space they subjectively experience conflict.

1386

1387 (D) The drift-diffusion model assumes choice and RT data can be modeled as a sequential
1388 sampling process; following an initial nondecision time (t), the decision process begins at starting
1389 point (z) and accumulates evidence at rate (v) toward one of two boundaries that determines the
1390 choice (in our case, approach (+) or avoid (-)); boundaries are separated by a distance (a).
1391 Parameters provide a fine-grained assay of behavior, such as any bias toward one choice (z),
1392 how rapidly evidence is integrated during decision formation (v) or the amount of evidence
1393 required before a choice is executed (a wider boundary denoting a more conservative criterion).
1394 States of high conflict might impact any or all of these parameters. We depict simulated
1395 schematics ($n=1000$ trials) of singularly changing the drift rate or the boundary separation. In
1396 each, we fixed a set of baseline parameters ($t=0.30$; $v=1$; $a=2$; $z=0.60$), and then increased or
1397 decreased v or a by 40%. Note that in each panel, there is a bias toward approach ($z>0.50$), and
1398 identifiably different features in the RT distributions of approach and avoid resulting from the
1399 parametric changes. For more in-depth examples, see Ratcliff and McKoon (2008).

1400

1401

1402

1403 **Figure 2 Graded approach-avoidance paradigm reveals fine-grained behavioral responses**
1404 **to conflict**

1405 (A) Participants approached (accept) or avoided (reject) offers pairing varying levels of monetary
1406 reward with varying levels of painful electric shock (communicated via size of relevant bar) with a
1407 single response during gradual onset of stimuli; see Methods for success, payout and error trials.

1408

1409 (B) Participants integrated reward (rew [b_1 , Eq. 1]) and cost (shk [b_2 , Eq. 1]) into choices, with a
1410 greater weighting of reward ($|rew| - |shk| > 0$), and a bias toward approach (int [b_0 , Eq. 1]) indicating
1411 reward sensitivity. Error bars are standard error of the mean across parameter estimates for each
1412 subject. *** $p < 0.001$, ** $p < 0.01$.

1413

1414 (C) Choice consistency (V_{choice}) was lower and median response time (med. RT) was longer for
1415 states identified (using logistic choice models) as high in conflict. *** $p < 0.001$.

1416

1417 (D) In states of high conflict, participants had a wider boundary (a), had a lower rate of evidence
1418 accumulation (v), had less of a bias toward approach (starting point (z)) and had a slightly shorter
1419 nondecision time (t). Boundary units are arbitrary "evidence", and drift rate is in units of "evidence"
1420 per second; starting point (z) is on a logit scale where positive values (i.e., > 0.50) are closer to
1421 approach boundary (see caption for Figure 1D). Nondecision time (t) is measured in seconds.

1422 Digitized violin plots contain 400 samples from parameter posterior. Summary data of posteriors
1423 and key comparisons are in Table 2-1. Vertical white lines span posterior HDI. *credible Bayesian
1424 difference between two parameters (θ_1, θ_2), i.e., $0 \notin \text{HDI}(D(\theta_1, \theta_2))$, where $D = [p(\theta_1 | X_1) - p(\theta_2 | X_2$
1425 $)]$.

1426

1427

1428

1429 **Figure 3 Interactive cross-modal collaboration associated with the decision boundary of**
1430 **the drift-diffusion model (DDM)**

1431 (A) Separate flicker rates applied to reward and cost stimuli afforded capture of steady-state
1432 visually evoked potential timeseries for reward (SS_{rew}) and cost (SS_{cst}). In the "symmetry"
1433 timeseries (SS_{sym}), higher values reflect greater symmetry (more equal power) between the two
1434 SS timeseries ($-1 * \ln|(SS_{\text{rew}} - SS_{\text{shk}})|$). Timeseries were averaged in early [0 to 1 s] and late [1 s to
1435 2 s] time windows relative to offer onset.

1436

1437 (B) Lateralized stimuli afforded capture of alpha-power timeseries relevant for reward (α_{rew})
1438 and cost (α_{cst}). In the "symmetry" timeseries (α_{sym}), higher values reflect greater symmetry
1439 (more equal power) between the two alpha timeseries ($-1 * \ln|(\alpha_{\text{rew}} - \alpha_{\text{shk}})|$). Timeseries were
1440 averaged in early [0 to 1 s] and late [1 s to 2 s] time windows relative to offer onset.

1441

1442 (C) Posterior parietal delta and frontal-midline theta power. Timeseries were averaged in early [0
1443 to 1 s] and late [1 s to 2 s] time windows relative to offer onset.

1444

1445 (D) The pre-ejection period (PEP) is recorded with combined impedance cardiography (ICG) and
1446 electrocardiography (EKG); shorter PEP indicates increased sympathetic beta-adrenergic
1447 myocardial contractility. Our contractility estimates, where higher values reflect greater cardiac-
1448 sympathetic drive ($\text{contractility} = -1 \cdot \ln(\text{PEP})$), were averaged across each heartbeat in a [0 to 2 s]
1449 time window relative to offer onset.

1450

1451 (E) Singular models for DDM parameters $\{a, v, z, t\}$ modeled by a single regressor (x_1 ; i.e., either a
1452 neural variable or contractility), separately for states of low and high conflict (Eq. 6). Six models
1453 improved fits beyond the baseline model in Figure 2D. Fits assessed relative to baseline with
1454 improvements in deviance information criterion ($-\Delta\text{DIC}$), positive values reflecting better fit.
1455 Double-headed (\leftrightarrow) arrow denotes an association that could be negative or positive.

1456

1457 (F) Cross-modal models for DDM parameters $\{a, v, z, t\}$ modeled by either additive or interactive
1458 models winnowed from the fits in Figure 3E. Additive models (empty circles) modeled DDM
1459 parameters by a neural variable (x_1) in addition to contractility (cont.), separately for states of low
1460 and high conflict; 16 regressors in total. Interactive models (circles with crosses) also included a
1461 third regressor for the product of the neural signal and contractility [Eqs. 7–8]. Six models
1462 improved fits beyond the best-fitting model in Figure 3E.

1463

1464 (G) Complement models (Eq. 9) asked if the fit of the best-fitting cross-modal model (which
1465 included α_{shk} ; marked "m1" in Figure 3F) could be improved by adding the complement (i.e.,
1466 set difference) of cross-modal models using neural variables that passed the singular model

1467 stage, using their best-performing forms (with or without interactions), marked with “m2” in Figure
1468 3F. Each model improved fits beyond the best-fitting model in Figure 3F. In the best overall fitting
1469 complement model (marked with *), DDM parameters were modeled by four regressors: α_{shk} ,
1470 α_{sym} , contractility and $\alpha_{sym} * \text{contractility}$.

1471

1472 (H) Proxy of variance explained (R^2) by best fitting baseline, singular, cross-modal, and
1473 complement models across varying RT bin sizes. Each trial’s RT was simulated using a Wiener-
1474 like process with relevant model parameters and regressors, and R^2 values were derived from
1475 Pearson correlations between RT bin medians (observed vs simulated).

1476

1477

1478

1479 **Figure 4 Dynamics of the best-fitting complement model**

1480 (A–D) Parameter posteriors from best-fitting (complement) model of DDM parameters. Most
1481 neural and cardiac-sympathetic relations involved the decision boundary (a). In both low- and
1482 high-conflict states, wider boundaries were related to greater desynchronization of α_{shk} ,
1483 greater symmetry in alpha (α_{sym}) and increased contractility. Unique to states of high conflict,
1484 the boundary showed additional positive association with the alignment of cross-modal signals
1485 ($\alpha_{sym} * \text{contractility}(\text{cont.})$). Digitized violin plots contain 400 samples from parameter posterior.
1486 Summary data of posteriors are in Table 4-1. Vertical lines span highest density interval (HDI) of
1487 coefficient posterior, and are white if HDI does not contain 0 (also marked with *), black otherwise.

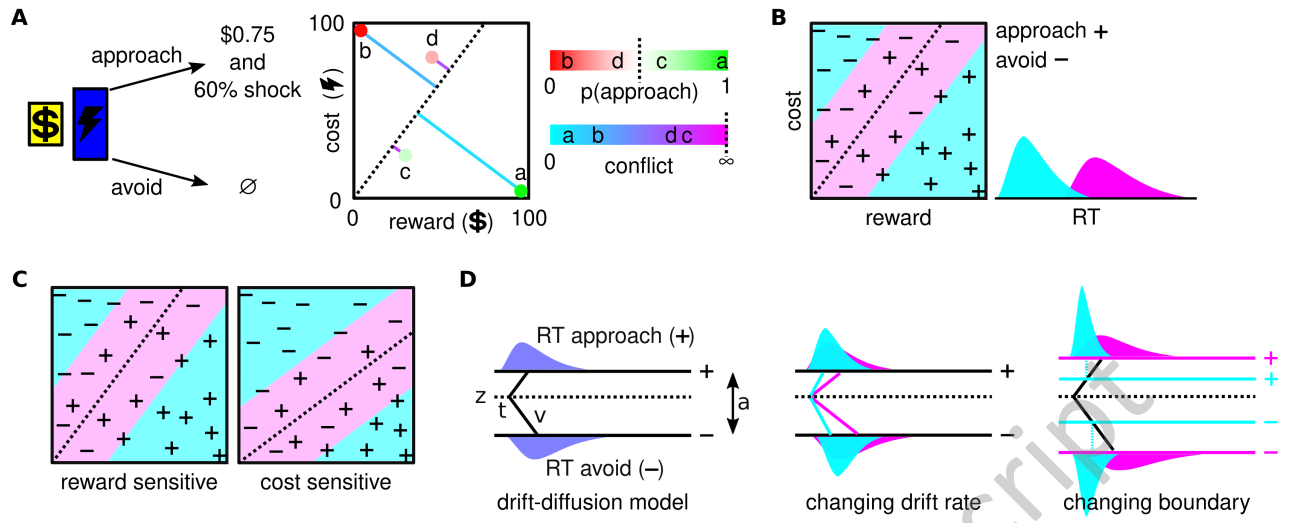
1488

1489 (E) Parameter posteriors from a model to discretize the neural and cardiac interactions associated
1490 with the decision boundary. Boundary is widest (relative to the baseline, low conflict, low late
1491 α_{sym} and low contractility— Δ boundary) in high conflict when α_{sym} and contractility are
1492 both high. + and - symbols respectively reflect high and low (for physiology signals, relative to
1493 participant medians). Digitized violin plots contain 400 samples from parameter posterior.
1494 Summary data of posteriors and key comparisons are in Table 4-2. Vertical lines span the highest
1495 density interval (HDI) of coefficient posterior and, are white if HDI does not contain 0. *** denotes
1496 this posterior was credibly larger than all others depicted, i.e., $0 \notin \text{HDI}(D(\theta_1, \theta_2))$, where $D = [p(\theta_1$
1497 $|X_1) - p(\theta_2|X_2)]$ for all possible values of θ_2 .

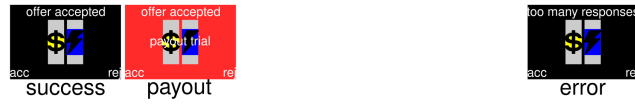
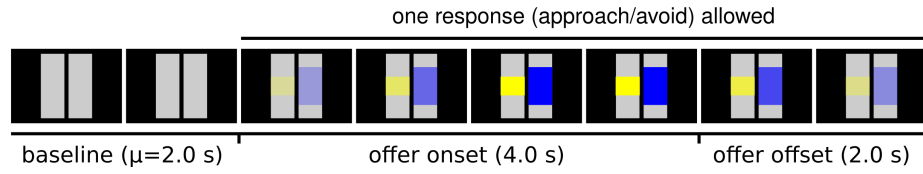
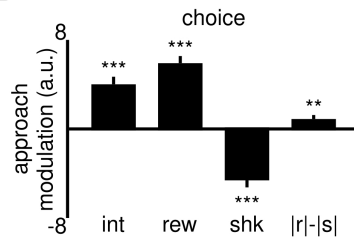
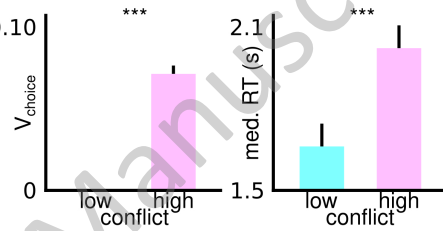
1498
1499 (F) Control models substituted proxy measures for local and global brain activity for all regressors
1500 featuring contractility in the best-fitting complement model. The model substituting contractility
1501 with global field power (GFP) was a slightly better fit. However, inspection of the parameters show
1502 opposing associations with the boundary (marked by black arrows). That is, GFP's interaction
1503 with α_{sym} was associated with a contraction of the decision boundary. Summary data of
1504 posteriors for the GFP control model in Table 4-2.

1505
1506 (G) Phase-angle timeseries of alpha contralateral to reward ($\alpha_{\text{rew}\theta}$ - top) and cost ($\alpha_{\text{shk}\theta}$ -
1507 bottom) in high conflict, averaged across subjects separately for trials that were higher (dark red)
1508 or lower (light red) than their median contractility.

1509
1510 (H) Summarizing phase coherence (absolute phase-angle value $|\theta|$) across early and late time
1511 windows, we see a three-way interaction whereby late coherence diminishes significantly in high
1512 contractility, and only in the alpha timeseries contralateral to reward.



JNeurosci Accepted Manuscript

A\$0.01 - \$1.50   min - max pain**B****C****D**